Annual Review of Analytical Chemistry

Quantum Cascade Laser–Based Vibrational Circular Dichroism Imaging for Chiral Biosensing

Michael Le,[1,*] Viviana Arrunategui Norvick,[1,*] Laurence Nafie,[2] and Yamuna Phal[1,3,4,5]

[1]Department of Electrical Engineering, Colorado School of Mines, Golden, Colorado, USA

[2]Department of Chemistry, Syracuse University, Syracuse, New York, USA

[3]Quantitative Biosciences and Engineering Program, Colorado School of Mines, Golden, Colorado, USA; email: yphal@mines.edu

[4]Quantum Engineering Program, Colorado School of Mines, Golden, Colorado, USA

[5]Colorado Clinical and Translational Sciences Institute, Aurora, Colorado, USA

Annu. Rev. Anal. Chem. 2026. 19:121–52

First published as a Review in Advance on February 27, 2026

The *Annual Review of Analytical Chemistry* is online at anchem.annualreviews.org

https://doi.org/10.1146/annurev-anchem-071625-085942

*These authors contributed equally to this article

Keywords

quantum cascade lasers, vibrational circular dichroism imaging, chirality, chiral biosensing, proteins, pharmaceutical drugs

Abstract

Vibrational circular dichroism (VCD) is an established chiroptical technique that probes molecular handedness via differential IR absorption of left- and right-circularly polarized light. Quantum cascade lasers (QCLs) have revitalized VCD spectroscopy by delivering high-power, narrowband mid-IR sources that, combined with polarization-modulation strategies, have dramatically improved VCD sensitivity and speed—enabling imaging that was not previously attainable. We review the instrumental design of QCL-based VCD imaging and demonstrate its application to spatially resolved chiral biosensing. By mapping VCD signals with micrometer resolution, one can detect and differentiate protein secondary structures, monitor enantiomeric purity in pharmaceutical compounds, and visualize pathological tissue features without labels. We discuss practical challenges, including cell-window birefringence, polarization-sensitive detection, and data processing, and propose optimized configurations for robust imaging. Finally, we outline future directions for QCL-VCD systems and their integration with nonlinear chiroptical techniques, highlighting the potential of QCL-VCD imaging to transform chiral analysis in biological and clinical contexts.

1. INTRODUCTION

Vibrational circular dichroism (VCD): differential absorption of left- and right-circularly polarized IR light by chiral molecules, providing stereochemical and secondary-structure information

Quantum cascade laser (QCL): semiconductor mid-IR source generating high-power, narrowband emission through cascading intersubband transitions, enabling tunable and coherent IR illumination

Circular dichroism (CD): the UV counterpart of VCD

Vibrational circular dichroism (VCD) has been an important tool for observing the chiral properties of molecules, with a wide range of applications from pharmaceutical development to cancer biology. Traditionally, VCD spectroscopy has faced several challenges, including low signal intensity and low signal-to-noise ratios (SNRs), which necessitate long acquisition times and highly sensitive detectors. The advent of quantum cascade lasers (QCLs) has reduced these problems by offering a coherent, high-intensity light source in the mid-IR region (5–25 μm). In this review, we provide a brief historical background of VCD and the technological precursors leading up to QCL-based VCD (QCL-VCD). We discuss the fundamentals of QCLs and their operation, as well as other components and theory critical for a complete QCL-VCD setup. We then describe the mathematical basis for extracting VCD spectra and assess how current research in semiconductors and digital processing is pushing the limits of QCL-VCD into the future. By bringing together current knowledge and recent advances in the field, this review demonstrates the promise of QCL-based VCD spectroscopy and imaging. **Figure 1** presents a timeline of the key developments that have paved the way toward QCL-VCD.

2. VIBRATIONAL CIRCULAR DICHROISM: BACKGROUND AND PRIMER

2.1. Vibrational Circular Dichroism

Both electronic circular dichroism (ECD or CD) and VCD are spectroscopic techniques that deal with chiral molecules, those with nonsuperimposable mirror image forms like a left and a right hand. However, they offer information in different parts of the electromagnetic spectrum. CD focuses on the UV region. It provides insights into the electromagnetic interactions within a molecule and can be used to study the secondary structure of proteins (e.g., α helix, β sheet) or

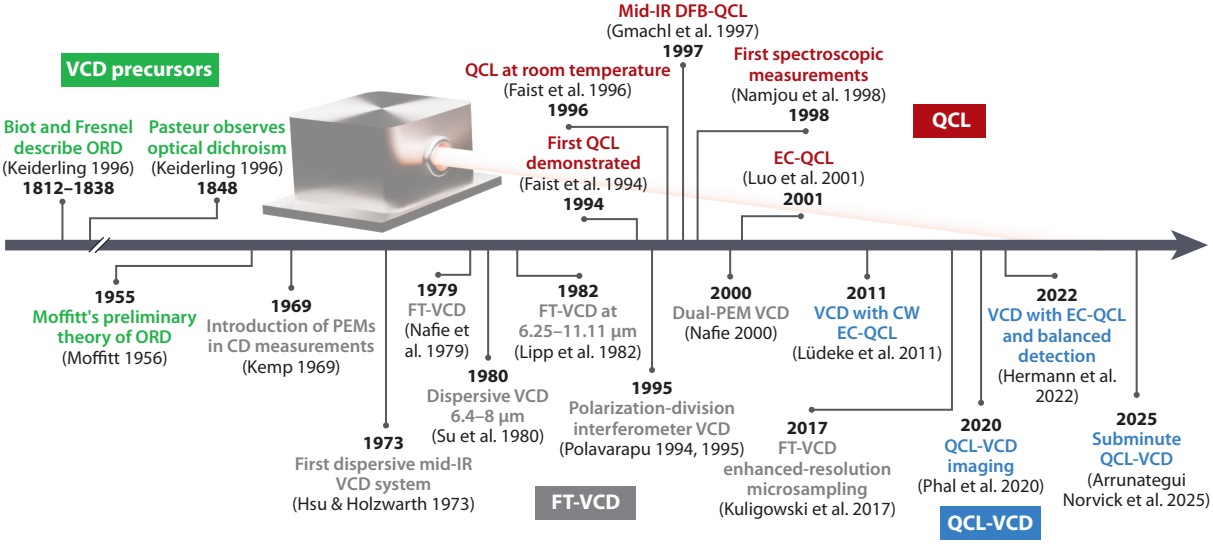

Figure 1

A timeline of key innovations relevant to the progression of QCL-VCD technology. Green denotes prior optical dichroism discoveries. Blue and red correspond to advances in the fields of QCL-VCD and QCL, respectively. Abbreviations: CD, circular dichroism; CW, continuous-wave; DFB, distributed feedback; EC, external cavity; FT-VCD, Fourier transform IR absorption–based VCD; ORD, optical rotatory dispersion; PEM, photoelastic modulator; QCL-VCD, quantum cascade laser–based vibrational circular dichroism.

Table 1 Major instrumental milestones in QCL-VCD and their impact on measurement capability

Instrumental update	Significance
Polarization-interferometric VCD system	Exploits differential phase measurements between orthogonal polarization channels to achieve high-sensitivity chiral detection and robust baseline stability
Dual-PEM FT-VCD system	Addition of a second PEM suppresses LB artifacts, enabling baseline-free VCD measurements in solid-state samples
Rotating stage integration	Continuous sample rotation averages out window-induced LB and LD effects, further stabilizing the baseline in solution-phase VCD
Introduction of QCL sources in mid-IR region	High-power, narrowband, and tunable lasers become available, dramatically improving VCD sensitivity and spectral power density
Single-PEM QCL-VCD proof of concept	First demonstration that a single-PEM-modulated QCL can record VCD in liquid samples, validating QCL as a viable VCD source
QCL-VCD imaging via raster scanning	Spatially resolves chirality by synchronizing QCL-VCD with micrometer-scale scanning, opening the door to two- and three-dimensional chirality maps
Subminute QCL-VCD spectroscopy	Combines rapid wavelength switching and advanced data processing to achieve real-time VCD spectroscopy

Abbreviations: CD, circular dichroism; LB, linear birefringence; LD, linear dichroism; PEM, photoelastic modulator; QCL, quantum cascade laser; VCD, vibrational circular dichroism.

larger macroscopic characteristics of the target molecule. VCD operates mainly in the IR region, and it directly probes the vibrational modes of bonds within the molecule. VCD offers a key advantage in providing information about the three-dimensional arrangement of these bonds due to its higher vibrational-mode sensitivity.

In order to understand how contemporary researchers arrived at QCL-VCD, we must first understand the technological building blocks and years of research that preceded it. The next section discusses pivotal QCL-VCD predecessors: optical rotatory dispersion (ORD), CD, dispersive VCD, Fourier transform IR absorption (FT-IR) spectroscopy, and FT-IR-based VCD (FT-VCD) (**Table 1**).

2.2. Vibrational Circular Dichroism Precursors: Optical Rotatory Dispersion and Circular Dichroism

ORD, which was originally theorized and experimentally observed by Jean-Baptiste Biot and Augustin-Jean Fresnel between 1812 and 1838, laid the foundation upon which all stereochemistry has been built (1). ORD describes the frequency-dependent rotation of planar-polarized light when interacting with an enantiomeric molecule.

In 1956, Moffitt (2) published his preliminary theory of the ORD of the α helix, one of the first mathematical models corroborating observed light rotation with the molecular α-helical structure of poly-γ-benzyl-L-glutamate and poly-α-L-glutamic acid (3). Contemporary ORD entered a renaissance in the early 1950s with the invention and widespread academic adoption of the first "modern" spectro-polarimeters and stable light source emitters, which enabled accurate rotation measurements of planar-polarized light in solution (1, 4, 5). These developments, along

with continually advancing instrumentation for measuring CD spectra, led to one of the first comprehensive CD spectra, reported by Greenfield & Fasman (5).

2.3. The Transition from Circular Dichroism to Vibrational Circular Dichroism

The studies performed by Greenfield & Fasman (5) and by contemporary researchers relied on basic, manually adjustable, or narrowly automated measurement devices to measure spectral CD modulation. These devices often consisted of a broad-spectrum visible/UV source coupled with longitudinal electro-optic modulators, principally nonlinear optical crystals made from potassium dihydrogen phosphate (KDP) (1, 5–7). These KDP crystals, while able to modulate linearly polarized light into the desired right- and left-circular polarization modes, were severely limited by their transmission spectrum and were generally opaque to the longer wavelength IR light required for VCD measurements (6). The advent of photoelastic modulators (PEMs) was critical to the advancement of VCD (8, 9). The ability to easily fabricate PEMs from various IR-transmissive materials allowed for a significantly broader wavelength range, and researchers were finally able to generate high-quality right- and left-circularly polarized IR light (6). Note that, until the introduction of PEMs, all measurements had been restricted to CD spectra between the UV and visible light regimes (~200–700 nm). VCD requires a much longer wavelength light source to observe vibrational-mode transitions of the target molecule. A more in-depth discussion of implementing PEMs in QCL-VCD systems is presented in Section 4, below.

2.4. Modern Vibrational Circular Dichroism Systems Preceding Quantum Cascade Lasers

FT-IR and dispersive spectroscopy are two methods of measuring VCD. Traditionally, both FT-VCD and dispersive VCD utilized a blackbody light source emitting across a broad mid-IR region (10, 11).

Rapid-scan FT-VCD, pioneered by Nafie et al. (12) and Nafie & Diem (13), relies on a Michelson interferometer that translates the optical wavelength into a function of mirror position and time. The interference resulting from the changing mirror position generates a low-frequency modulation, typically in the range of 1–3 kHz, known as Fourier modulation. Following the interferometer, the light passes through a linear polarizer and then a PEM, which produces modulating circularly polarized light in the range of 37–50 kHz. Subsequently, the light is focused on a detector, typically a liquid nitrogen–cooled photoconductive (PC) detector such as an HgCdTe (MCT) detector. The signal is then processed through lock-in amplifiers that demodulate both the high-frequency differential polarization absorbance and the Fourier-modulated signal. Some companies, such as BioTools, employ additional digital processing techniques to replace lock-in amplifiers. **Figure 2*a*** presents a schematic of a typical FT-VCD system. Another notable implementation is the polarization-interferometric VCD system developed by Polavarapu et al. (14, 15), which exploits differential phase shifts between orthogonal polarization channels to achieve greatly enhanced sensitivity in chiral measurements.

A full scan in rapid-scan FT-VCD yields two interferograms, a high-frequency differential polarization absorbance and a low-frequency Fourier-modulated signal that fluctuates according to the path-length difference determined by the interferometer's moving mirror. The Fourier transform (FT) of each interferogram generates a spectrum spanning a broad range of wavelengths. The differential absorbance FT signifies the difference in absorbance between left- and right-circularly polarized light, which is divided by the Fourier-modulated FT representing the average light intensity and acting as a normalization factor (10, 17–21). Consequently, integration of a Michelson interferometer with advanced digital processing enables rapid-scan FT-VCD to

simultaneously collect a signal across all wavelengths (i.e., multiplexed) without extending data collection times when expanding the observed bandwidth. Typically, FT-VCD scans cover the entire mid-IR region (~800–1,800 cm^{-1}). To enhance the SNR, multiple scans are averaged, and complete FT-VCD measurements with a resolution of 4–8 cm^{-1} generally require minutes to hours depending on the VCD strength and the sample transmission throughput. However, higher-resolution scans require larger path-length differences in the Michelson interferometer, resulting in longer acquisition times (11).

Dispersive VCD uses a monochromator to filter the broadband source into a single wavelength of the desired resolution. The broadband light is directed into a slit, where it is reflected onto a

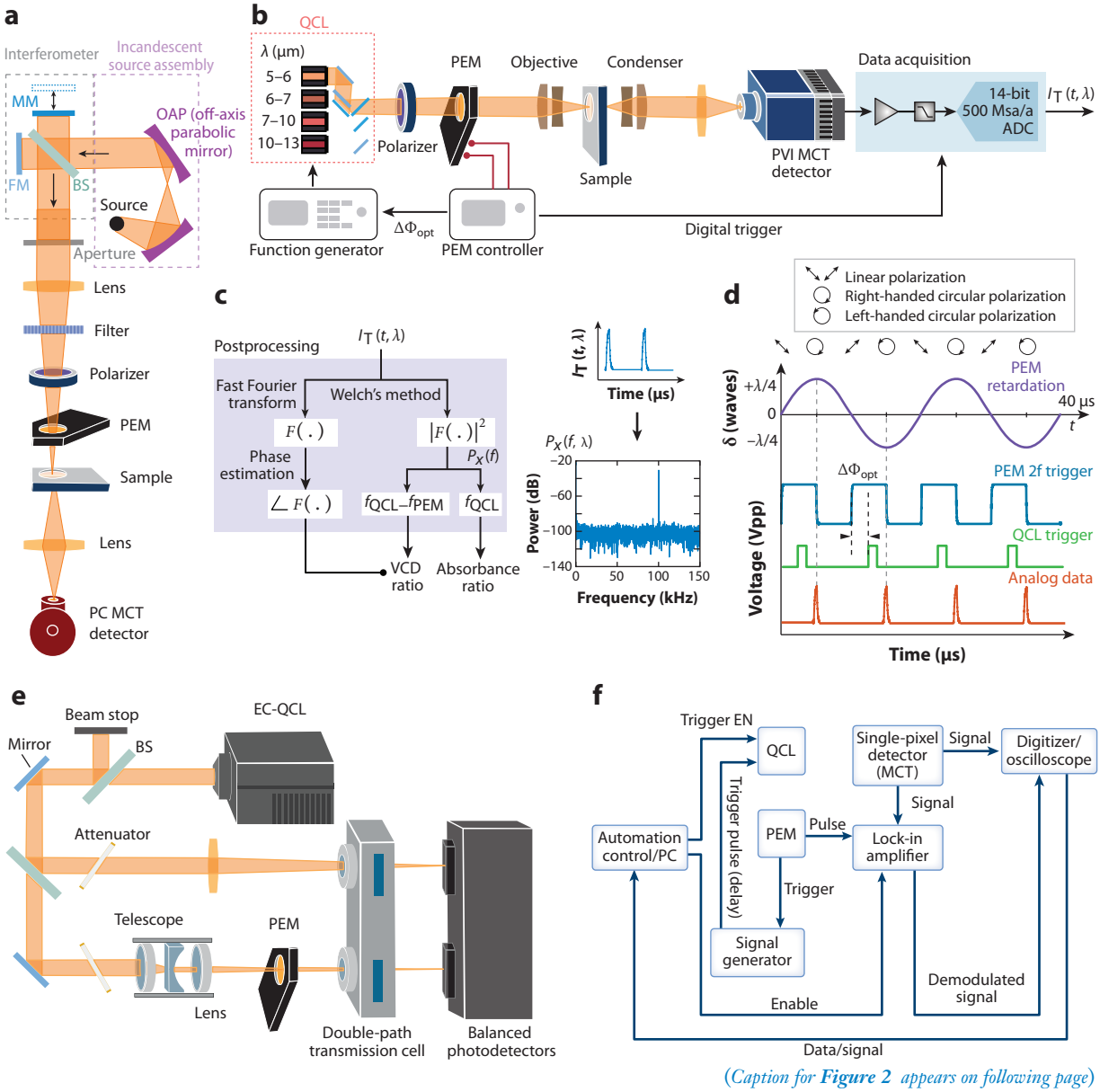

(*Caption for* ***Figure 2*** *appears on following page*)

Figure 2 (*Figure appears on preceding page*)

(*a*) A typical FT-VCD scheme. A broadband source is collimated and passed through a Michelson interferometer consisting of a beam splitter (BS), a fixed mirror (FM), and a movable mirror (MM). The beam is then passed through a focusing lens, filter, polarizer, and PEM and then through the target sample and a final focusing lens before the MCT detector. (*b*) Schematic of a multiple-wavelength QCL-based VCD spectrometer, including the following components: QCL, PEM, polarizer, and photovoltaic MCT detector. A back-end data acquisition and control system uses a digital trigger to align QCL pulses to the PEM and a high-speed digitizer card to capture and process the amplitude-modulated signal acquired by the detector (16). (*c*) (*Left*) Postprocessing workflow for extracting frequency components from time-series data, $I_T(t, \lambda)$. (*Right*) Power spectral density visualization, highlighting the frequency components that ensure accurate signal demodulation and noise reduction for reliable VCD signal extraction. (*d*) Time-series plots showing PEM retardance and associated light polarization states, PEM trigger signal, calibrated QCL trigger signal with phase shift $\Delta\Phi_{opt}$, and detector output of laser pulses triggered by the QCL trigger. (*e*) Schematic of a balanced QCL-VCD setup. The EC-QCL output is attenuated using a BS, directing half the light into a beam stop. The remaining beam is reflected by a mirror and guided into another BS, dividing it into reference and sample beam pathways. Both beams pass through attenuators. The reference beam is focused by a ZnSe lens through a double-path transmission cell onto the detector. Meanwhile, the sample beam is directed through a cage system with a telescope to reduce its diameter before being focused by a ZnSe lens through the PEM and the double-path transmission cell onto the detector. Detection is performed by a balanced detection module with two thermoelectrically cooled MCT photodetectors. (*f*) A typical automation/control block diagram for a QCL-VCD system. Abbreviations: EC, external cavity; FT-VCD, Fourier transform IR absorption–based VCD; MCT, HgCdTe; PC, photoconductive; PEM, photoelastic modulator; PVI, photovoltaic IR; QCL, quantum cascade laser; VCD, vibrational circular dichroism.

grating that diffracts the light, allowing a single wavelength to exit through a secondary slit. This mechanism enables dispersive VCD to sequentially scan individual wavelengths across the desired range. Following the monochromator, the light passes through a polarizer and a PEM. After PEM modulation, the light passes through the sample and is detected by a mid-IR detector, such as an MCT detector (19, 20, 22). All dispersive VCD methods incorporate double modulation, where the light is modulated at a lower frequency with a chopper placed before the PEM. The acquisition time for dispersive VCD varies depending on the spectral band measured, increasing for larger bandwidths. For instance, at a resolution of 10 cm^{-1}, dispersive VCD may require 15–30 min to measure amide I and II bands ($\sim$200 cm^{-1}). Complete scans often necessitate repetition and averaging to enhance the SNR.

Rapid-scan FT-VCD has dominated the commercial field of VCD because of its multiplexing advantage, but it faces limitations that make alternative methods preferable on the basis of setup and applications. Dispersive VCD is favored for measuring with aqueous solutions, where the spectral windows of water feature high absorbance and restrict the information that can be acquired over a broad range. Dispersive VCD can be optimized for narrow spectral bands that provide the most useful information. The broad range of FT-VCD cannot filter or avoid spectral windows of water, which reduces signal intensity and ultimately the SNR. To achieve a higher SNR, FT-VCD often requires averaging over several thousand scans, resulting in increased acquisition time and nullifying its multiplexing advantage. Additionally, VCD setups comprise PEMs and lenses that feature inherent wavelength dependence. Consequently, the reliance of FT-VCD on wavelength multiplexing can lead to chromatic effects, thereby compromising bandwidth and spectral output. In contrast, dispersive VCD, with its narrower spectral range, can circumvent such chromatic effects and avoid the dispersion limitations of lenses and prisms (10, 11, 23).

2.5. Quantum Cascade Laser–Vibrational Circular Dichroism Systems and Configurations

Traditional FT-VCD spectrometers employ a globar source and a Michelson interferometer for broadband mid-IR generation, followed by one or two PEMs for polarization modulation and dual lock-in detection to extract the weak chiral signal (**Figure 2*a***). In QCL-VCD systems (**Figure 2*b***) (see the sidebar titled Principles of QCL-VCD Imaging), the broadband lamp and

PRINCIPLES OF QCL-VCD IMAGING

QCL-VCD imaging extends point spectroscopy by mapping chiral absorption across a two-dimensional field of view. Instead of recording a single VCD spectrum, the sample is raster scanned (or imaged with a focal-plane array) while polarization is modulated at each pixel. The resulting pixelwise differential absorption of left- versus right-circular polarization yields a spatially resolved map of molecular chirality. Key challenges include maintaining a stable optical path length, preserving modulation purity across the scan, and isolating the weak VCD signal from the much larger unpolarized background. Successful implementations demonstrate micrometer-scale resolution and open new avenues for label-free visualization of protein secondary-structure distributions in cells and tissues.

interferometer are replaced by one or more narrowband, tunable QCLs, whose output is stepped (or pulsed) in place of an interferogram and synchronized to the PEM with optimized PSD calibration (16). Matching of each laser pulse to the PEM drive enables improvement of acquisition speeds by an order of magnitude, and the vastly higher mid-IR power reduces integration times—from minutes to seconds—while maintaining lock-in or digitizer-based detection. When paired with beam-scanning optics or focal-plane arrays, this architecture ultimately enables true VCD imaging (**Figure 2*d***). The modulated beam may be detected by a single MCT detector, whose output feeds both lock-ins (one referenced to the QCL repetition or chopping for DC transmission, one to the PEM for AC VCD). Although digital processing and boxcar integration can suppress laser intensity noise by up to fourfold (24), these processing steps depend significantly on averaging of the signal pulses and do not completely eliminate the noise contributed by the QCL intensity fluctuations (25, 26).

Although QCLs offer many advantages over other IR lasers, they face multiple problems arising from their lasing mechanisms. As a result of QCLs' wavelength-dependent gain material, QCLs typically exhibit maximum intensity in the middle of their emitted spectral range, with weaker power at the spectral edges. This wavelength-dependent spectral power density causes variation in laser intensity, which leads to detector saturation in certain spectral regions while decreasing intensity and thus sensitivity in other regions (21, 27, 28). To mitigate this issue, wavelength-selective filters are employed to adjust power levels in different spectral regions. However, laser intensity noise is not as easily resolved, requiring changes to detector configuration in order to be minimized (29, 30).

Balanced detection (**Figure 2*e***) enables full cancellation of intensity fluctuations through the detection of a reference signal. This is achieved by splitting the laser power into two paths, the reference path and the sample path, which will modulate the VCD signal. Here, the VCD-modulated signal is subtracted from the in-phase reference signal, effectively canceling out the common noise (the laser intensity fluctuations) while preserving the VCD signal itself (31, 32). Balanced detection uses two detectors that are matched in transimpedance, voltage responsivity, and detectivity to produce a high common-mode rejection ratio (29).

Balanced detection with QCLs has found widespread application in absorption spectroscopy, demonstrating a significant noise reduction capability (30, 33, 34). Studies have shown that it can reduce noise levels by a factor of 20 compared with single-detector setups and by a factor of 2 compared with premium commercial FT-IR systems (27). In external cavity (EC-)QCL-VCD systems, balanced detection can improve noise by a factor of 4 compared with single detection and produces comparable noise levels to commercial FT-IR while reducing acquisition time by a factor of 6 and increasing resolution by a factor of 2.5 (32). In balanced detection schemes, the current signals at the detector are directly subtracted from one another in a subtractive circuit.

Because direct subtraction requires synchronization of both signals to effectively cancel out all laser fluctuations, the optical path of each signal must be matched. Additionally, effective noise cancellation requires that both signals have identical or similar power at the detectors.

Matching the reference and VCD signal power at the detectors can be achieved through adjustments to the optical setup or the electrical circuit. For instance, introducing a similar sample or a neutral density filter into the reference path can reduce the reference signal amplitude to match the absorption observed in the VCD signal path (27, 30). Although balanced detection can improve noise by a factor of 20, changes in the VCD signal during measurement make perfect power matching difficult. To enable better power matching, a laser noise canceller circuit is employed, as it adds a circuit splitter with negative feedback to the traditionally used subtractive circuit (35, 36). In this setup, the reference signal amplitude is initially larger than the VCD signal at detection. The variable current splitter then adjusts the reference signal current to match the VCD current amplitude. The splitter operates with a negative-feedback loop, splitting the reference current such that the reference and VCD DC signals at the output of a transimpedance amplifier, used for voltage conversion, are zero. The addition of this circuit enables up to 50 dB suppression with balanced detection. However, while balanced detection improves laser intensity noise, it does not address shot noise. Shot noise from the reference signal and from the VCD signal are statistically independent, resulting in their cumulative addition within the subtractive circuit. Consequently, the shot noise is 3 dB higher than that of the VCD signal alone (36, 37).

2.6. Signal Acquisition in Quantum Cascade Laser–Vibrational Circular Dichroism Systems

Most spectroscopy systems employ a well-known method of signal acquisition, utilizing a lock-in amplifier to extract phase-sensitive information from the carrier signal (38–41). In the context of VCD, lock-in amplifiers demodulate the modulated signal at the difference or sum frequency related to the difference in absorption between right- and left-circularly polarized light (32, 42–45). The mathematical basis for this difference is discussed further in Section 5 (see also Equations 3 and 4). This technique enhances the SNR by selectively amplifying the carrier signal at the PEM modulation frequency f_{PEM}, from which we can obtain the relevant VCD spectra of the sample, $\Delta A_{\mathrm{VCD}}(\lambda)$.

Figure 2*c* depicts an alternative postprocessing workflow for extracting frequency components from time-series data, $I_{\mathrm{T}}(t, \lambda)$. Welch's method is applied to the time-series data to extract the f_{QCL} and $f_{\mathrm{QCL}} - f_{\mathrm{PEM}}$ frequency components. The method involves splitting the time signal into overlapping segments, applying a window function to each segment, and calculating the periodogram $P_x(f, \lambda)$ from the time-series data $I_{\mathrm{T}}(t, \lambda)$. A significant consideration in QCL-VCD design involves determining the appropriate synchronization method between the QCL and the PEM (**Figure 2*d***). If a QCL operating in pulse mode cannot be pulsed in with a trigger input from a signal generator or directly from the PEM output, other methods of QCL synchronization must be considered. **Figure 2*f*** depicts a generic automation/control schema for a QCL-VCD system.

We briefly discuss two other methods of extracting phase-sensitive VCD spectra; however, they are less prevalent in the field. Polarization scrambling, proposed by Nafie (42) and Cheng et al. (9), implements a secondary PEM modulated at a frequency slightly different from that of the first PEM, directly after the target sample. VCD spectra are inherently sensitive to spurious and undesirable noise introduced throughout the complex light path. In the case of QCL-VCD systems, issues like nonideal polarization are minimized thanks to the QCL's inherent coherent and linear polarization characteristics. However, to further reduce the noise floor and consequently improve the SNR of the entire system (noise such as PEM, sample, and mirror birefringence),

the second PEM placed directly after the sample modulates the entirety of the VCD spectrum and birefringent baseline. The second PEM, in essence, reports only the birefringent baseline of the system (42). Experiments have shown that, for FT-VCD, significant improvements to baseline noise—in some cases near zero—have been achieved (18, 21, 46, 47). For a complete derivation for dual-PEM theory, see Reference 9, and for a contemporary experimental derivation of the dual-PEM Stokes parameters via Stokes polarimetry, see Reference 48.

Linear dichroism (LD): differential absorption of orthogonal linear polarizations by anisotropic media, requiring removal for accurate VCD spectra

Advanced modulation strategies—dual-PEM and polarization scrambling—are directly transferable to QCL-VCD systems. By placing a second PEM immediately after the sample and driving it at a frequency offset from the first, one can selectively tag and remove birefringence and linear dichroism (LD) artifacts (18, 46, 47). Polarization scrambling, wherein a secondary PEM modulates at a slightly different frequency, further isolates the pure VCD response from parasitic baselines (9, 42). Multifrequency lock-in detection then cleanly separates the true VCD term from all other modulation components, reproducing the near-zero baselines achieved in FT-VCD and promising equivalent performance in QCL-VCD (48).

Extending these schemes into a microscope format, using galvanometric beam scanners or mid-IR focal-plane arrays, will finally enable truly label-free, micrometer-scale chirality maps (44, 45). Early imaging prototypes, however, revealed that residual LD (from sample mounts and window birefringence) must be addressed (44, 49). Systematic optimization of QCL tuning protocols, PEM alignment and drive, detector matching, and cell-window design will be critical to suppress artifacts and deliver high-fidelity QCL-VCD imaging for biological and clinical applications. In the next section, we turn to a detailed examination of the individual components—QCLs and different configurations, PEMs, and detector architectures—exploring their various configuration types, performance trade-offs, and integration strategies for optimal VCD imaging.

3. FUNDAMENTALS OF QUANTUM CASCADE LASERS: THEORY, DESIGN, AND APPLICATION

3.1. Background

Lasers emit coherent light through the process of stimulated emission. Electrical power is pumped into the laser's gain material to excite electrons into a higher energy state, emitting photons when they return to their lower energy state. Photons can stimulate excited electrons to produce more photons with the same wavelength. These photons propagate in a resonant cavity with partially reflective edges that reflect a portion of the light back into the cavity, enabling further stimulated emission. However, for lasing to occur, most of the electrons must be in excited states (population inversion). This ensures that stimulated emission dominates over the absorption of photons by lower-energy electrons (50).

Interband (conduction to valence band) transitions produce photons whose wavelength is determined by the bandgap of the material. QCLs are unique because of their use of intersubband transitions. QCLs emit photons when electrons in the conduction band move from a higher energy level to a lower energy level in the same or a neighboring quantum well (QW). Since the amount of and space between energy levels of a QW can be controlled by its dimensions, QCLs can be engineered to emit in the mid- to far-IR region (3–100 μm) using the same material systems that confine interband lasers to the near-IR region (51).

Although the idea of utilizing intersubband transitions for optical gain was first proposed in 1972 by Kazarinov & Suris (52), in 1994 Faist et al. (53) became the first to realize a QCL. A QCL consists of two sections, the gain section and the injection section, which are repeated for 10 to 100 periods; 20 to 30 repetitions are more commonly employed (54). **Figure 3*a*** shows the Feynman diagram for the gain–injection energy well structure.

The injection region comprises a superlattice that is slightly doped and serves as an electron reservoir to inject carriers into the active region. This superlattice consists of repeating QWs with thin barrier thicknesses that enable efficient electron tunneling and increase QW wavefunction overlap to produce minibands of energy levels spanning the injection region. An electric field is

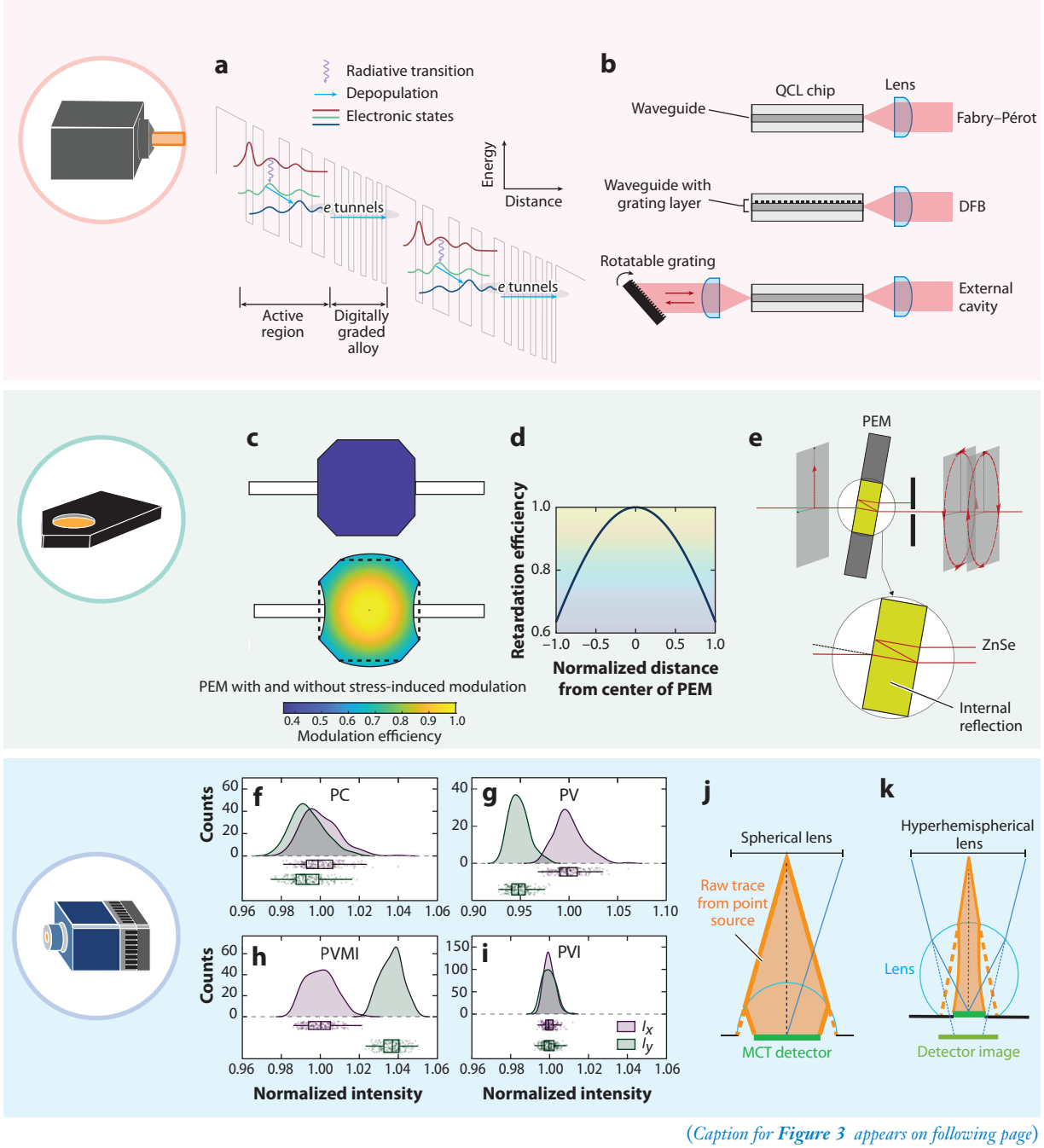

(*Caption for* ***Figure 3*** *appears on following page*)

Figure 3 (*Figure appears on preceding page*)

(*a*,*b*) QCLs. (*a*) Schematic energy band diagram of a QCL. An electric potential is applied to a structure composed of alternating quantum wells and barriers within the conduction band. In the active region, electrons emit photons. In the injector region, electrons tunnel through to the excited energy state of the following active region. (*b*) Typical QCL configurations. (*Top*) A basic Fabry–Pérot resonant cavity (waveguide). (*Middle*) DFB architecture consisting of a typical resonance cavity, but with an integrated optical grating layer that serves as an optical filter for resonant modes within the cavity. (*Bottom*) EC-QCL architecture. The inclusion of an external rotatable grating allows for a broader tuning range and enhanced mode stability compared with DFB architectures. (*c*–*e*) PEMs. (*c*) Retardation efficiency of a PEM without stress (*top*) and under stress (*bottom*). (*d*) Retardation efficiency plotted against normalized distance from the center of the PEM, showing the variation in optical retardation with spatial position. (*e*) Positioning of the PEM at a slight angle to minimize back reflections. The angled placement ensures that any reflected light is deflected out of the main beam path and directed onto a beam stop, preventing interference before the beam continues through the optical setup. (*f*–*k*) Photodetectors. Differential response of various detector configurations for orthogonal polarization orientations at 0° and 90°: (*f*) PC, (*g*) PV, (*h*) PVMI, and (*i*) PVI. The output intensity distribution of 0° and 90° polarized light illumination recorded by the different detectors is denoted I_y and I_x, respectively. (*j*,*k*) Optical immersion configurations for MCT detectors. (*j*) A spherical lens provides full detector immersion with minimal spherical aberrations compared with (*k*) a hyperhemispherical lens. However, a hyperhemispherical lens configuration increases the effective light area capture and improves the efficiency of the detector. Abbreviations: DFB, distributed feedback; EC, external cavity; MCT, HgCdTe; PC, photoconductive; PEM, photoelastic modulator; PV, photovoltaic; PVI, photovoltaic immersion; PVMI, photovoltaic multiple immersion; QCL, quantum cascade laser.

applied over the QCL, creating a staircase-like structure in the conduction band that enables the electrons of lower energy levels in the injection region to be injected into the higher energy levels in adjacent QWs of the active region (51, 55, 56).

The active region of a QCL consists of cascaded QWs, which can either form a superlattice or possess barriers with sufficient thickness to minimize QW wavefunction overlap, thereby resembling a multiple-quantum-well (MQW) structure. MQW structures are commonly used with a three-QW design. Such designs depend on a direct transition to produce a photon. Nonradiative relaxation mechanisms are used to quickly scatter electrons from the lower and ground states into the injection region such that the electron population in the lower energy states is smaller than in the higher energy states, thus ensuring population inversion (51, 54). Superlattice designs are used because they scatter photons efficiently into the injection region. Superlattice designs such as the bound-to-continuum design enable the electron to go from a high energy level into a miniband of energy levels, enabling a broader wavelength output compared with the three-QW design (51, 57). For all QCL active region designs, optical transitions in QWs are bounded by selection rules. Consequently, stimulated emission in QWs will produce photons with electric fields perpendicular to the layers of QWs, leading to transverse-mode-polarized light (50).

3.2. Types of Quantum Cascade Lasers and Vibrational Circular Dichroism Applications

When the gain region of the QCL emits photons, the photons are coupled into an optical resonant cavity. This cavity, known as a Fabry–Pérot (FP) cavity (**Figure 3*b***), consists of a waveguide that confines the light and partially reflective facets that reflect part of the light back into the cavity. The reflected light with wavelengths that are integer multiples of the optical round-trip length of the cavity constructively interferes with itself, forming a standing wave. Consequently, the FP cavity acts as a wavelength filter where the optical path length, which depends on the length and refractive index of the waveguide material, controls the output wavelengths (50). FP-QCLs are the simplest and earliest QCL configuration (53, 58). Since refractive index changes with temperature, FP-QCLs use temperature tuning to change the wavelength outputs. However, the FP cavity supports multiple wavelengths with narrow mode spacing on the order of 1 cm^{-1}, while the laser gain bandwidth is 100–200 cm^{-1} (51). Consequently, FP-QCLs are limited to multimode applications such as FT-IR spectroscopy (59) and are not useful in applications where control over individual wavelengths is required.

Distributed feedback (DFB-)QCLs enable single-mode operation by integrating a filter onto the FP-QCL chip. This design incorporates a grating with periodic refractive-index changes (**Figure 3*b***), which acts as an optical filter for resonating modes within the FP cavity (51). The grating's period length and refractive index determine wavelength filtering and, consequently, can be tuned with temperature. The first DFB, developed by Faist et al. (60) in 1997, featured a pulsed single-mode DFB at 5.4 and 8 μm with a temperature tuning range of 60 nm between 100 and 320 K, followed by a DFB with a 40 nm tuning range between 200 and 300 K (61). DFB-QCLs were first used in spectroscopy applications in 1998 (62) and are useful because of their small size, single-mode emission, and mode hop–free tuning (57). However, DFB-QCLs offer a limited tuning range of 10–25 cm^{-1} with external temperature control (63) or 2–5 cm^{-1} with current-induced Joule heating (57). DFB-QCL arrays have been developed to increase the spectral range; arrays of 32 DFB-QCLs demonstrate a tuning range of 0.7–1.8 μm at 8 μm (90–220 cm^{-1}) (64, 65). However, DFB arrays encounter challenges such as laser variability, leading to inconsistent threshold currents, slope efficiency, output power, and single-mode selection (64).

EC-QCLs overcome limited tunability through the placement of a diffraction grating externally to the QCL chip (**Figure 3*c***). EC-QCLs use a combination of temperature control and external grating rotation to tune the output wavelength (57, 66, 67). Early EC-QCL designs faced spectral range limitations, prompting the development of bound-to-continuum active region designs to achieve broader wavelength output (51, 68, 69). Additionally, QCLs commonly use the quasi-Littrow configuration, where light is partially coupled back into the QCL chip to enable higher output power. Modern EC-QCLs exhibit a spectral range exceeding 400 nm (185 cm^{-1}) within the range of 4.4–5 μm (70) or 0.8–1.45 μm (120–150 cm^{-1}) within the range of 8–11 μm in continuous-wave (CW) mode (71–73). Pulse-mode operation achieves larger tuning ranges of up to 2.2 μm (265 cm^{-1}) (74) and requires less power than CW operation. However, pulse mode suffers from pulse-to-pulse intensity fluctuations and has larger linewidths and smaller power output than CW mode (50). Larger wavelength ranges can be achieved by combining multiple EC-QCL modules; EC-QCLs of 7.6–11.4 μm (438 cm^{-1}) have been demonstrated (75), with commercial demonstration even beyond 12 μm.

EC-QCLs are preferred in QCL-VCD setups because of their single-mode operation and broad wavelength range. CW-mode EC-QCLs are used in dispersive VCD systems because of their high power, ease of use with PEMs, and absence of the pulse-to-pulse fluctuations observed in pulse-mode EC-QCLs (29, 49, 76, 77). Pulse-mode EC-QCLs are also employed in dispersive VCD systems as a result of their cost-effectiveness, reduced cooling requirements, and minimized heat generation at both sample and detector (44, 78). Furthermore, pulse-to-pulse fluctuations can be effectively eliminated through balanced detection (32, 43).

3.3. Quantum Cascade Lasers Versus Traditional Lasers for Vibrational Circular Dichroism Applications

Traditional methods for VCD measurement rely on blackbody light sources to emit mid-IR light. However, these light sources emit unpolarized light over a broad range, necessitating additional filters and polarizers to attain linearly polarized light at distinct wavelengths (10, 11, 20). Specifically, dispersive VCD depends on a monochromator to isolate light at a specific wavelength. Achieving a finer resolution with a monochromator requires a grating with higher dispersion or a reduction in the size of the output slit, both of which degrade the signal amplitude and subsequently the SNR. Moreover, dispersive VCD and FT-VCD require grid polarizers to convert the unpolarized light into linear polarization, further diminishing the signal amplitude (79). QCLs circumvent the necessity for monochromators and polarizers because of their inherent linear polarization and

INSTRUMENTATION STRATEGIES FOR VCD IMAGING

Adapting VCD to imaging requires the combination of a mid-IR source, a polarization modulator, a sample-scanning stage, and a detector in an integrated microscope-like platform. QCLs deliver the narrowband, high-power, mid-IR light needed for rapid pixel acquisition. Polarization modulation (typically via a PEM) must be synchronized with the scanning motion to ensure that each image pixel samples the full polarization cycle. Detection schemes range from single-point MCT detectors with fast galvanometric mirrors to emerging focal-plane arrays that capture entire frames of modulated IR light. Optimization of beam shaping, modulation frequency, and detector reset speed is critical to balance spatial resolution, spectral fidelity, and acquisition time—paving the way for routine VCD imaging in chemical and biomedical research.

design, which include built-in grating structures or external cavities that enable wavelength filtering (51). Other mid-IR lasers such as QW interband diode lasers and interband cascade lasers can operate only between 3 and 4 μm at room temperature (80). In contrast, QCLs offer a distinct advantage in that they can emit linearly polarized light at designated wavelengths across the entire mid- to far-IR region (81–84) (see the sidebar titled Instrumentation Strategies for VCD Imaging).

Additionally, QCLs can achieve much higher power per wavelength compared with their thermal light source counterparts. VCD signals are four to six orders of magnitude weaker than classical absorbance measurements (32). Consequently, a suitable SNR requires a low noise floor, which is usually achieved by averaging hundreds to thousands of spectrum scans to increase the acquisition time (11). QCLs emit up to 10^4 times more power at a given wavelength than do thermal light sources, enabling higher signal power to reach the detector (76). For instance, QCL-VCD systems can have 2,400 times more signal at a resolution of 4 cm^{-1} in comparison to traditional FT-IR (49). The additional power is particularly beneficial near 1,640 cm^{-1}, where there is strong absorption caused by the HOH bending band of water. Additionally, QCLs can be used to increase the optical path length of the sample by a factor of five, avoiding near-total IR absorption while increasing the sensitivity and decreasing the limits of detection (27). Overall, the high power of QCLs enables experiments and samples that have higher absorbance or require greater sensitivity.

4. OPTICAL AND ELECTRONIC SYSTEM DESIGN

The optical system design is crucial for sensitive VCD measurements using QCLs. This section delves into the design considerations and specific components of the optical system to achieve optimal performance for QCL-VCD spectroscopy.

Linear birefringence (LB): optical anisotropy causing differential phase delay between orthogonal linear polarizations, producing artifacts in VCD measurements

4.1. Photoelastic Modulators

A PEM is a variable waveplate that uses mechanical stress to induce linear birefringence (LB) and thus periodic phase. A PEM consists of an isotropic optical element and a piezoelectric transducer, which applies a periodic stress at the resonant frequency of the optical element (8). The retardation pattern across the optical element depends on its shape, commonly either a bar or an octagon.

For a bar-shaped optical element, both the PEM and the transducer are the length of half the resonance wavelength. This design ensures that the application of a periodic stress at the resonant frequency creates a standing wave in the optical element. The refractive index parallel to the mechanical stress, n_x, changes, while the refractive index perpendicular to the mechanical stress, n_y, remains relatively unchanged. This produces birefringence, where the phase difference

between the horizontally and vertically polarized light is given by Equation 1:

$$\Delta\phi = \frac{2\pi}{\lambda}(n_x - n_y) \times t_z, \qquad 1.$$

where λ is the laser wavelength and t_z is the thickness of the optical element. Peak retardation occurs at the center of the optical element and varies sinusoidally along the direction of the applied stress.

For an octagonal optical element, the shape symmetry allows stress applied in one direction to induce an opposing stress perpendicular to that direction. This changes the refractive indices, n_x and n_y, in opposite directions, thereby producing a larger birefringence for the same applied mechanical stress as a bar-shaped PEM. The retardation varies sinusoidally in both the x and y directions, approximated by Equation 2, thereby creating a symmetric retardation pattern across the optical element (**Figure 3*c,d***):

$$\eta_r = \frac{2}{\pi x_n} \sin\left(\frac{\pi}{2} x_n\right), \qquad 2.$$

where η_r is the retardation efficiency and x_n is the normalized distance from the PEM center. Additionally, an octagonal optical element can withstand a stronger force compared with a bar shape before reaching the breaking point (85).

PEMs operate at a single frequency determined by the material of the optical element as a result of their resonant nature. Although PEMs are limited to one operating frequency, the resonant operation requires significantly less power than the application of a static stress. Operating at the resonant frequency allows the applied force to create a standing wave that can oscillate indefinitely within the optical element, depending on the damping (Q factor). With Q factors in optical materials ranging from 100 to 10,000, resonant operation requires significantly less force—by a factor of Q—compared with the application of a static stress (8). Consequently, higher retardation values can be achieved at lower powers before the breaking point of the optical element is reached.

PEMs are crucial for varying waveplate retardance, producing light states that transition efficiently between linear and circular polarizations. They operate on the principle of the photoelastic effect (i.e., piezoelastic effect), wherein stress induced on the PEM material produces a change in the refractive index (**Figure 3*c,d***). Aside from PEMs, this effect can be used to measure applied force (transducer), record audio (piezoelectric microphone), or generate high voltage and induce sparking across an air gap (a simple handheld lighter). In a PEM, the device is operated in the inverse: Voltage is applied across the crystal, inducing an interlattice strain. The slight distortion of the lattice results in a change in the refractive index. To maximize this photoelastic effect, PEMs are operated at the resonant relaxation frequency of the lattice structure (on the order of kilohertz). An alternating current is applied across the PEM at this resonant frequency, resulting in a maximized antisymmetric distortion of the crystalline lattice and, thus, a maximized antisymmetric distortion in the refractive index (86–88).

Rudimentary glue joint PEMs were first designed and constructed by Badoz et al. (89) and others (90); later improvements by Kemp (8) involved fusing resonant $\lambda/2$ transducers and an optical element. Kemp also proposed the use of PEMs in place of KDP crystals for generating alternating right- and left-polarized circular dichroism measurements. A suitable CD-IR (0.55–13 μm) PEM was subsequently developed by Cheng and colleagues (9, 86). It was composed of a zinc selenide (ZnSe) optical element bonded to two fused silica (quartz) transducers.

Modern PEMs for use in QCL-VCD systems have not changed significantly in the past decade. Devices such as the Hinds Instruments PEM 200 II/ZS50 consist of an octagonal ZnSe optical element bonded to two fused silica transducers. This device offers a widely tunable $\lambda/4$ wavelength

retardation range (2–18 μm) and nominal operating frequencies of 30–80 kHz, readily achievable by commercial benchtop lock-in amplifiers.

In a QCL-VCD system, the PEM's fast axis should be oriented at 45° to the incident linear polarization to enable phase modulation into right- and left-circular polarization states. Additionally, achieving synchronization between the PEM and pulse-mode QCLs is essential because of its small laser duty cycle. Precise alignment between the QCL's output and the PEM's modulation ensures accurate polarization modulation, preventing elliptical polarization states. In practice, this is done by aligning the QCL trigger to the PEM at the correct retardance. To minimize interference effects introduced by the PEM (**Figure 3*e***), the PEM is placed slightly off-normal to the incoming beam. This placement reduces the effect of internal reflection inside the element, and the addition of an aperture or beam stop after the PEM prevents scattered light from hitting the sample.

4.2. Detector Types

Evaluation of detector configurations is crucial to ensure a uniform response across varying polarization states of incident light, which is necessary for precise chiral measurements. In this section, we compare detector configurations such as PC, photovoltaic (PV), photovoltaic multiple immersion (PVMI), and photovoltaic immersion (PVI) to identify the optimal choice for different experimental setups.

We focus primarily on achieving a uniform polarization response (a p_x/p_y ratio close to one) and minimizing signal loss and polarization effects through careful optical alignment and the use of a low-numerical-aperture lens. The output intensity distribution of 0° and 90° polarized light illumination recorded by different detectors is denoted I_y and I_x, respectively; the signal intensity is normalized to I_x for each case. Both PC and PVI detectors have a near-polarization-independent response, and PVI detectors manifest much narrower and overlapping distributions. Considering the uniform response and high repeatability, PVI is currently the ideal detector type choice for general polarization measurements.

Other parameters that should be taken into account for polarization characterization studies are the effect of detector size and the responsiveness that is directly related to the detector noise floor. Furthermore, noise effects at each stage of the design, including photon, preamplifier, and thermal noise, can affect system performance (16, 42).

4.2.1. Photoconductive detectors. QCL-VCD photodetectors based on PC semiconductor materials operate by absorbing light, generating nonequilibrium-state electrical carriers. In a simple bulk material configuration, two electrodes are placed at either end of the substrate. Incident radiation is absorbed by the material, and the absorption and carrier emission lead to a reduction in the electrical resistance across the two electrodes. The choice between intrinsic and extrinsic materials is crucial in determining the performance of these detectors. Intrinsic materials involve interband transitions within a pure bulk material that occur between the valence and conduction bands, driven by photon energy exceeding the bandgap energy. Examples of bulk materials include lead salt, cadmium sulfide, and mercury cadmium. Extrinsic materials, in contrast, incorporate engineered impurities to create additional bandgap energy levels, typically doped with elements such as arsenic, gold, and indium. Silicon and germanium substrates are commonly used, particularly doped versions, and are well-suited for long-wavelength IR (>20 μm). However, thermal excitation poses challenges, especially in extrinsic materials because of their small-bandgap nature, leading to noise introduced by additional carriers (in addition to typical environmental noise and induced noise due to quantization). Fortunately, this issue is reduced for most QCL-VCD applications as a result of the QCL's typical sub-10-mW laser intensity (44, 91, 92).

4.2.2. Photovoltaic and photovoltaic immersion detectors. PV detectors differ from PC detectors in that, instead of a measured change in electrical resistance (and a resultant current change given a constant voltage input), PV detectors operate on a current induced by the absorption of a photon (93–95). In a typical PV semiconductor heterostructure, a photon is absorbed, causing excitation of an electron out of the valence band and into the conduction band of the material (93, 96). The movement of the electron from the valence band creates a hole. The surrounding electrons from the valence band move to fill this hole, causing an electron–hole propagation through the valence band and, thus, an induced current within the material. A typical material choice is a p-type silicon wafer doped with an n-type dopant (phosphorus, arsenic, antimony, bismuth, or another Group V substrate–compatible element) (97, 98).

To improve the efficiency of PV detectors for use in the mid-IR range, two significant changes must be made to the general architecture. Typically, silicon-based PV bandgaps are too large for mid- to far-IR photon energies. To overcome this problem, MCT is grown epitaxially (via molecular-beam, liquid-phase, or vapor-phase epitaxy) on a bulk CdZnTn substrate or GaAs with a CdTe buffer layer (97, 99). MCTs come in either an uncooled or an actively cooled (liquid nitrogen) configuration. However, recent advances in MCT heterostructure engineering have reduced or completely eliminated the need for cooling (99, 100). This configuration allows for operating regions in the range of 1–12 μm with the possibility to cut to wavelength and remove signal exposure up to a desired wavelength. To improve the exposure and sensitivity of the MCT sensor, the sensor can be fully optically immersed in either a spherical or a hyperhemispherical IR-compatible lens (BaF_2, CaF_2, ZnSe, or silicon) (**Figure 3*j*,*k***), increasing the total light capture area. However, the use of optically immersing lenses introduces nonnegligible aberrations in focal-plane array detectors that must be accounted for in postprocessing.

5. MUELLER MATRIX FORMALISM

The Stokes–Mueller formalism is a powerful mathematical framework used to describe the polarization properties and the interactions of light within optical systems. It provides a comprehensive way to characterize how light changes its polarization state and intensity as it passes through various optical components and interacts with materials (optical train) (42, 101).

5.1. Optical Setup

The theoretical model of an FT-VCD spectrometer in standard transmission configuration is well-known (42, 102). We can extend this formulation to provide a mathematical framework for a QCL-VCD system by using a coherent time-varying pulsed light source (44, 103–105). The polarization state of an optical beam is represented in the Stokes vector, **S**, as

$$\mathbf{S} = \begin{Bmatrix} I \\ Q \\ U \\ V \end{Bmatrix} = I_0(t,\lambda) \begin{pmatrix} I_{\mathrm{T}} \\ I_{0^\circ} - I_{90^\circ} \\ I_{45^\circ} - I_{135^\circ} \\ I_{\mathrm{R}} - I_{\mathrm{L}} \end{pmatrix}, \qquad 3.$$

where I is the total intensity and sum of all the orthogonal polarizations of the QCL pulse, Q and U are the differences in the linear polarization components, and V is the difference between right- and left-handed polarizations (RCP − LCP). To more accurately represent the time-varying nature of a QCL operating in pulse mode, we can represent **S** as the product $I_0(t,\lambda)$ with a normalized Stokes vector, where λ is the wavelength. Dealing with the time-varying nature of QCL pulses is beyond the scope of this section, and more research to classify the QCL in a VCD system is necessary (see the sidebar titled Adapting the Mueller Matrix Formalism for QCL-VCD Systems).

ADAPTING THE MUELLER MATRIX FORMALISM FOR QCL-VCD SYSTEMS

When a CW QCL is intensity-modulated by a mechanical chopper (or when a pulsed QCL is used), the time-dependent laser power enters the Stokes vector as an additional sinusoidal term. In practice, the first element of the Stokes vector becomes $I_0(t, \lambda) \approx I_0(\lambda) \cdot \sin \omega_{QCL}$, and each downstream Mueller matrix must carry that modulation through the optical train.

In addition, the PEM imposes a second polarization modulation at its own frequency. The detected signal therefore contains a DC term, a PEM–frequency difference signal (the true VCD), and a component at the QCL repetition or chopping frequency. A complete Mueller matrix description must account for both modulation depths and their relative phases, typically by expanding each sinusoidal term in Bessel function series, so that sum and difference terms can be cleanly demodulated and separated in the lock-in acquisition.

Below, we assume that I is a time-varying function of λ and the QCL angular frequency rate ω_{QCL} [e.g., $I_0(t, \lambda) \approx I_0(\lambda) \cdot \sin \omega_{QCL}$] (16, 42, 44, 106). The strictly linear interaction of an optical device with a beam of light can be described as a transformation of an incident Stokes vector $\mathbf{S_i}$ into an emerging Stokes vector $\mathbf{S_o}$ ($\mathbf{S_o} = M\mathbf{S_i}$, where M is the Mueller matrix that is characteristic of the optical device or system). We might also think of the Mueller matrix as a linear operator acting on a Stokes vector. As such, the order in which Mueller matrices are applied is mutable. Without any instrumental polarization, the matrix M equals the identity matrix, and $\mathbf{S_o} = \mathbf{S_i}$. The transformation of $\mathbf{S_i}$ by a sequence of optical devices is given by the linear operation of a Mueller matrix on the incident Stokes vector, including the rotation matrices arising from the angles between their planes of incidence. This theory is already well-established, so we simply point out the changes in the theory that are directly applicable to accommodating the time-varying nature of the laser pulses.

The Mueller matrix representations for the critical optical elements used in a single-detector setup are approximately described in Equation 4, which neglects any nonlinear interference and interaction effects, including the polarization change due to the lenses:

$$\begin{aligned} \boldsymbol{I_T}(\lambda) &= \boldsymbol{M_D}(\alpha)\boldsymbol{M_X}(\lambda)\boldsymbol{M_{PEM}}[45^\circ, \alpha_M(\lambda)]\boldsymbol{M_P}(0^\circ)\boldsymbol{S_0}(f_{QCL}, \lambda), \\ &= \frac{I_0(\lambda)}{4}\, 10^{-A''(\lambda)}\left(1 + 2J_1[\alpha_M^0(\lambda)]\mathrm{CD}(\lambda) + J_0[\alpha_M^0(\lambda)]\right), \end{aligned} \quad 4.$$

where $\boldsymbol{S_0}(f_{QCL}, \lambda)$ is the Stokes vector for the input QCL source beam, with pulse repetition rate f_{QCL} and peak intensity $I_0(\lambda)$. The individual Mueller matrices for the system can be represented sequentially from right to left with a polarizer, $\boldsymbol{M_P}(\lambda)$; a PEM, $\boldsymbol{M_{PEM}}(f_{PEM}, \lambda)$; the sample, $\boldsymbol{M_X}(\lambda)$; and a detector, $\boldsymbol{M_D}(\alpha)$.

Rather than focus on the full derivation of the Mueller matrix formalism, we discuss only the aspects that make the QCL-VCD formulation different from traditional FT-VCD systems. For instance, the detector Mueller matrix is given by

$$\boldsymbol{M_D}(\alpha) = \begin{pmatrix} 1 & (p_x^2 - p_y^2)\cos 2\alpha & (p_x^2 - p_y^2)\sin 2\alpha & 0 \end{pmatrix}. \quad 5.$$

Note that while $\boldsymbol{M_D}$ is a Mueller matrix, which is typically a 4×4 matrix, it can measure only the intensity of the final Stokes vector, $\mathbf{S}_{f0}$. That is, we do not know the intensity of either the right- or left-circularly polarized signal, merely their difference. The detector also possesses differential responses in both the x and y axes relative to the detector, p_x and p_y, as discussed above (**Figure 3*f–i***). We can also determine why it is beneficial to minimize $p_x - p_y$. If $p_x = p_y$, we can further simplify the detector expression so that all but the first term is zero.

Therefore, with laser modulation, the transmitted intensity consists of two main terms that are relevant for the VCD signal:

$$\boldsymbol{I}_{\mathbf{T}}(\lambda) = \boldsymbol{I}_{\mathbf{DC}}(f_{\mathrm{QCL}}, \lambda) + \boldsymbol{I}_{\mathbf{AC}}(f_{\mathrm{QCL}} \pm f_{\mathrm{PEM}}, \lambda). \quad 6.$$

We solve for the VCD spectrum $\Delta A_{\mathrm{VCD}}(\lambda)$ as follows:

$$\Delta A_{\mathrm{VCD}}(\lambda) = \frac{1}{1.1513\, J_1[\alpha_{\mathrm{M}}^0(\lambda)]} \left[\frac{\boldsymbol{I}_{\mathbf{AC}}(\lambda)}{\boldsymbol{I}_{\mathbf{DC}}^{\mathbf{0}}(\lambda)} \right]. \quad 7.$$

Circular birefringence (CB): differential phase retardation between left- and right-circularly polarized light, underlying vibrational optical rotation measurements

5.2. Samples and Nonlinear Contributions

The most commonly used Stokes–Mueller formulism presented above is formulated for neat liquids or solution-phase samples, generally neglecting the influence of LB introduced by cell windows. With the recent interest in development of VCD imaging techniques, this formalism needs to be revisited, as the contribution of LB cannot simply be neglected. Instead, solid-state VCD measurements must explicitly account for LB arising within the crystalline samples themselves. The following Mueller matrix–based analysis both clarifies solid-phase sampling and extends liquid-/solution-phase analyses to include window-induced birefringence.

A typical solid-phase sample, X, with both linear and circular anisotropies can be written in exponential form as a Mueller matrix:

$$M_{\mathrm{S}}(\lambda) = 10^{-A''(\lambda)} \left(1 - F(\lambda) + \tfrac{1}{2} F^2(\lambda) - \ldots \right). \quad 8.$$

Here, $F(\lambda)$ is the first-order sample matrix, whose nonzero elements represent the various anisotropic effects. The first-order sample matrix could be interpreted as indicating the optical composition of one, two, or multiple layers of solid aligned in the light path:

$$F(\lambda) = \begin{pmatrix} 0 & \mathrm{LD}(\lambda) & \mathrm{LD}'(\lambda) & -\mathrm{CD}(\lambda) \\ \mathrm{LD}(\lambda) & 0 & \mathrm{CB}(\lambda) & \mathrm{LB}(\lambda) \\ \mathrm{LD}'(\lambda) & -\mathrm{CB}(\lambda) & 0 & -\mathrm{LB}'(\lambda) \\ -\mathrm{CD}(\lambda) & -\mathrm{LB}(\lambda) & \mathrm{LB}'(\lambda) & 0 \end{pmatrix}, \quad 9.$$

where CB refers to circular birefringence. In this framework, both LB and LB′ quantify phase delay (birefringence) between orthogonal linear polarizations: LB refers to the refractive-index difference along the ±45° axes, while LB′ describes the contrast between the 0° and 90° axes. Physically, each produces a phase shift,

$$\Delta\phi = \frac{2\pi}{\lambda_0} (n_{\mathrm{slow}} - n_{\mathrm{fast}})\, l,$$

that alters the effective light speed c/n along the fast and slow axes.

Similarly, CB captures phase retardation between right- and left-circular polarizations by treating them as fast and slow modes, respectively. In contrast, LD and LD′ measure differential absorbance along those same axes: LD leads to stronger absorption along the ±45° axis, whereas LD′ reflects preferential absorption along the 0°/90° axis.

Typically, for most solution-phase and other cases, first-order approximation [i.e., the $1 - F(\lambda)$ term from Equation 8] is sufficient to represent the sample completely. With an ideal detector, the total intensity would exclude any contribution from birefringence terms, and the signals for CD, LD, and LD′ could be easily separated by the differing factors. The second-order contribution—including its full angular dependence—serves as the master equation for an enhanced description of the total intensity, where second-order CB and CD terms are negligible. A Mueller matrix

constructed at this level comprehensively describes optical effects in both solid-state samples and liquid-phase cells whose windows exhibit LB. This detailed model improves routine CD measurements in solution by accounting for baseline distortions introduced by LB and LB′ at any point in the optical train. Finally, rotation matrices are employed to project each anisotropic effect into the laboratory frame and capture orientation dependence. However, such Mueller matrix formulations inherently treat the sample response as a polarization-averaged ensemble and do not explicitly resolve the coupled field propagation of left- and right-circularly polarized components through multilayer or dispersive interfaces. To capture these interference- and thickness-dependent artifacts—particularly those arising from high-numerical-aperture focusing, birefringent windows, or stratified films—a full transfer matrix approach is required. Here, the field amplitudes for right- and left-circularly polarized light are propagated and solved independently across each interface (150).

6. APPLICATIONS OF QUANTUM CASCADE LASER–VIBRATIONAL CIRCULAR DICHROISM

6.1. Biological Samples: Proteins and Peptides

Unlike traditional IR or ECD spectroscopy, VCD exhibits greater variability in sign patterns and peak positions across frequency, making it uniquely capable of separating the spectral fingerprints of proteins and peptides (107) (**Table 2**). To interpret these complex spectral patterns, multivariate statistical methods such as principal components analysis and factor analysis have been applied to decompose VCD spectra into common band-shape components (**Figure 4*a***) that correlate quantitatively with α-helix and β-sheet content (108–110). In particular, the amide I region of VCD spectra shows distinct differences in sign, shape, and relative intensity between α helices and β sheets. Additional structural information can be extracted from the amide II and III regions, although their features tend to be broader and less distinct than those of amide I (111–113). Moreover, pilot studies suggest that cancerous tumor cells display altered VCD signatures—particularly in the amide I band—relative to healthy tissue (subpanel *ii* of **Figure 4*b***), opening the possibility of label-free cancer diagnostics based on secondary-structure biomarkers (114, 115).

Small synthetic peptides provided the clean testbeds that established modern VCD–secondary-structure relationships. This research revealed that right-handed α helices produce a positive amide I couplet with a negative amide II band, while β-sheet-rich chains show weaker, largely

Table 2 Key application areas for QCL-VCD imaging with the required spatial resolution

Application area	Sample type	Spatial resolution	Primary benefit	Reference(s)
Biomolecular structure	Proteins, peptides	10–50 μm	Distinguish α-helix/β-sheet content in situ	117–120
Pharmaceutical screening	Chiral APIs, intermediates	50–100 μm	Rapid absolute-configuration determination, high sensitivity	128, 129
Pathology and histology	Tissue sections, biofilms	5–20 μm	Label-free mapping of aberrant protein structures	114, 115
Astrobiology and space	Meteorite analogs, soils	100–500 μm	In situ chirality detection for biosignature assessment	129–133
Materials science	Polymers, crystalline films	1–10 μm	Map orientation and composition in anisotropic media	134

Abbreviations: APIs, active pharmaceutical ingredients; QCL-VCD, quantum cascade laser–based vibrational circular dichroism.

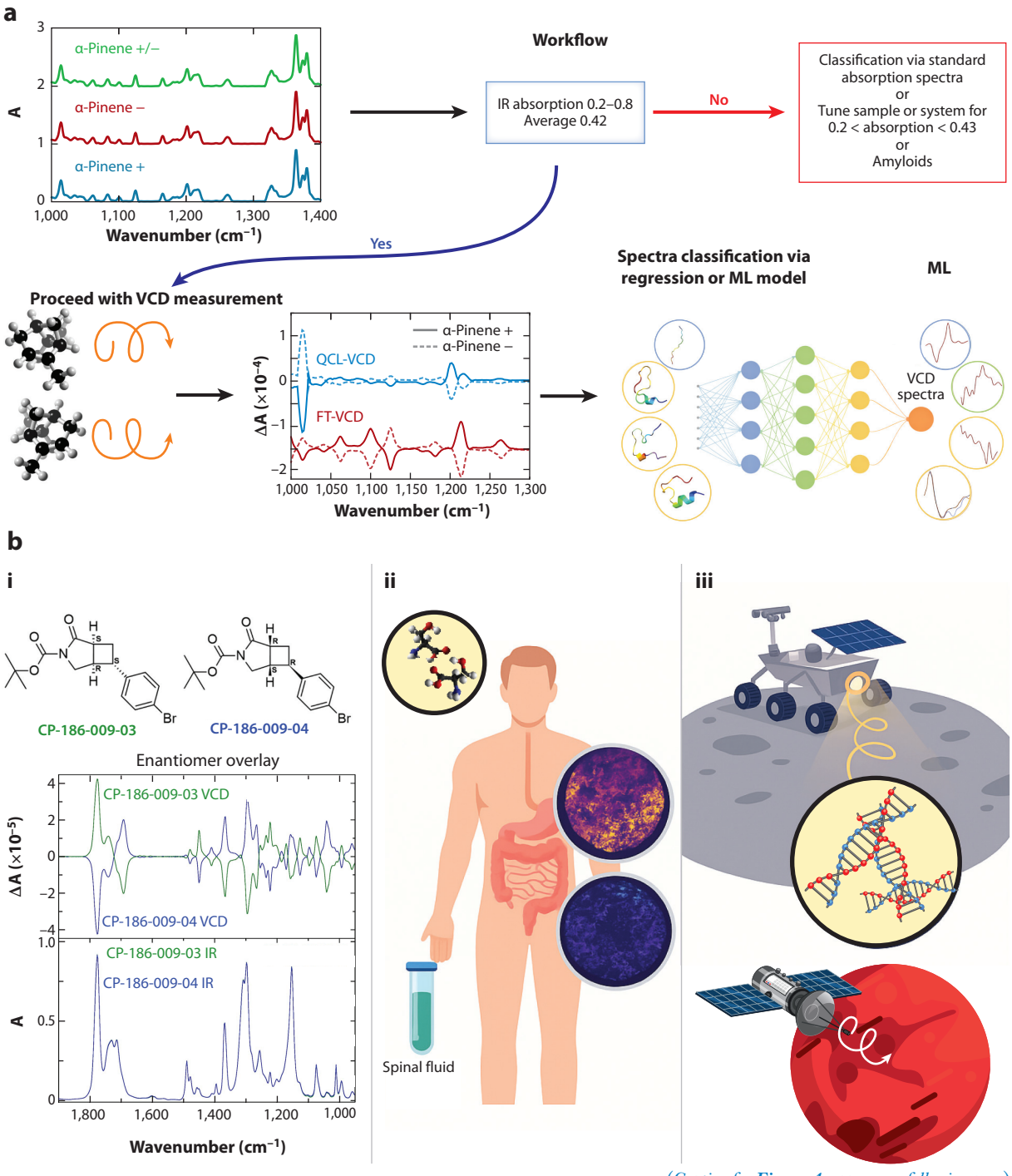

(*Caption for* ***Figure 4*** *appears on following page*)

Figure 4 (*Figure appears on preceding page*)

(*a*) Typical workflow for conducting VCD measurements. For a given biological spectral measurement, the typical IR absorption range should be between 0.2 and 0.8 (20–80% absorbance). For a maximized VCD signal, the absorption should be between 0.2 and 0.43. Once these conditions are satisfied and linear absorption measurements of the sample corroborate with known spectra, VCD measurements may be taken. There are some exceptions to the rule, as is the case for amyloid fiber or similar structures, where absorption values can be much higher than the typical 0.2–0.8. (*b*) Applications of VCD imaging techniques. (*i*) VCD can be useful in novel drug development to determine the absolute configuration of compounds, enantiomeric ratios of synthesized chemicals, and so forth. (*ii*) VCD can be used in histology and pathology to identify cancerous tissues or abnormal proteins, as in colorectal cancers. It has also shown success in identifying proteins in spinal fluid with a strong correlation to Alzheimer's disease. (*iii*) In space resources and space exploration, VCD has been proposed for use in analyzing the chemical composition of lunar and asteroid soils to identify key materials. Abbreviations: FT-VCD, Fourier transform IR absorption–based VCD; ML, machine learning; QCL, quantum cascade laser; VCD, vibrational circular dichroism.

negative amide I signals with split amide II features (107). These benchmark signatures continue to guide VCD analyses, enabling reliable secondary-structure assignments in complex and dynamic proteins. VCD offers higher specificity than FT-IR or ECD, allowing it to resolve overlapping structural contributions and correct misinterpretations based solely on frequency shifts, as in growth factors, keratin, and glycoproteins (116–118). VCD is also well-suited for monitoring subtle conformational changes arising from changing environmental factors, such as increased antiparallel β-sheet content in phosvitin at low pH, which FT-IR spectroscopy failed to detect accurately (119–121).

6.2. Biological Samples: Nucleic Acids

VCD can be used to analyze the chiral structures of nucleic acids (122). DNA adopts multiple conformations, including the right-handed A and B forms and the left-handed Z-DNA helix, each of which gives rise to distinct VCD spectral signatures in the phosphate and base-stretching regions. VCD enables differentiation of these forms on the basis of distinct spectral features, particularly differences in the C=O stretching region (approximately 1,550–1,750 cm^{-1}) (123). It can also detect changes in nucleotide sequence and monitor structural responses to external factors such as the presence of transition metals (124). These applications support the use of VCD in studies of conformational changes and sequence-dependent variations in DNA.

6.3. Pharmaceutical Compounds

Chirality is a fundamental property in drug development, as different enantiomers can exhibit significantly different biological activities. A notable example is thalidomide, whose R-enantiomer functions as a sedative while the S-enantiomer is associated with severe teratogenic effects, including birth defects. Given that around two-thirds of marketed drugs are chiral, ensuring enantiomeric purity is essential for pharmaceutical safety and efficacy (125). VCD plays multiple roles in chiral analysis, enabling both absolute stereochemical determination and deeper insight into the molecular mechanisms underlying chiral recognition and separation. As the demand for precise chiral characterization continues to grow, VCD's sensitivity, versatility, and compatibility with both solution and solid-state forms make it an increasingly valuable complement to established analytical methods.

VCD has emerged as a powerful technique for determining the absolute configuration of chiral compounds. While X-ray crystallography is commonly used for this purpose, VCD offers a faster, more cost-effective, and more sensitive alternative, especially for noncrystalline or low-quantity samples (122, 126). VCD measurements rely on comparison with reference spectra, typically calculated via density functional theory, a quantum mechanical atomistic simulation method, or known from other measurements. In cases where the stereochemistry is unknown, VCD paired

with simulation provides an efficient route for assignment. In AstraZeneca's development of neurokinin-3 antagonists, VCD was used to assign chirality through smaller, computationally manageable intermediates—a valid approach when chiral centers remain unchanged (127). VCD can also determine the absolute configuration in solid-state forms, including crystalline and amorphous materials, making it especially useful when solution-based methods are hampered by poor solubility or other limitations (128). Beyond absolute configuration, VCD has been employed to elucidate chiral separation on cellulose- and amylose-based stationary phases, which revealed opposite-backbone handedness and enantiomer-dependent differences in binding strength and inclusion depth, thereby providing detailed molecular insight into enantioselectivity (subpanel *i* of **Figure 4*b***).

6.4. Space Applications

The search for extraterrestrial life remains a central goal in the field of astrobiology. Among the most promising biosignatures are amino acids and potential bacterial microfossils, both of which have been identified in certain meteorite classes. These findings suggest that biologically relevant molecules and possibly traces of microbial life can survive interplanetary transport and persist over geological timescales. Detecting such compounds beyond Earth would provide important evidence for prebiotic chemistry or biological activity elsewhere in the Solar System.

Missions such as Mars sample return, Europa Clipper, and Dragonfly reflect growing interest in in situ investigations of potentially habitable environments. These efforts require compact and reliable instruments capable of identifying molecular structures under extreme conditions. In particular, chiral molecules such as amino acids require methods that can resolve enantiomeric composition, which is critical for assessing the likelihood of biological versus abiotic origin.

VCD can effectively analyze the composition and stereochemistry of organic and inorganic materials in laboratory settings. Its sensitivity to molecular chirality makes it amenable to the identification of asymmetric compounds of potential biological relevance.

As interest in direct analysis of extraterrestrial samples increases, the need for field-deployable methods for chirality detection becomes more pressing. QCL-based VCD systems offer a path toward this goal, with the potential to support remote characterization of enantiomeric compounds and guide sample selection for return or further study.

6.4.1. Extraterrestrial amino acids. One of the most distinctive features of terrestrial biology is homochirality, namely the consistent use of left-handed amino acids and right-handed sugars in living organisms (129). Although this molecular asymmetry is essential for biomolecular function, its origin is not well-understood (130). Several hypotheses suggest that homochirality may have arisen from asymmetric physical processes such as circularly polarized light from stars (131, 132), interaction with chiral mineral surfaces, or parity-violating β decay.

The detection of enantiomeric excesses in amino acids from certain carbonaceous meteorites supports the idea that such asymmetries originated extraterrestrially and were later amplified on early Earth (132, 133). These findings contribute to the broader hypothesis that the molecular building blocks of life could have a cosmic origin.

Amino acids are considered strong candidate biosignatures in astrobiology because of their biological relevance and the potential for abiotic synthesis in various planetary environments. Their chirality provides an important metric for distinguishing between abiotic and biotic origins. As such, the ability to detect and characterize amino acids in situ, particularly with respect to their enantiomeric composition, is essential for assessing the potential presence of life beyond Earth (subpanel *iii* of **Figure 4*b***).

6.4.2. Bacterial signatures. While the preference for homochirality offers insight into the chemical origins of life, the detection of bacterial signatures may provide direct evidence of past biological activity. Fossilized microbial structures are among the earliest records of life on Earth, with examples extending back more than three billion years (135). These fossils are often preserved as mineralized biofilms or as sedimentary features such as stromatolites.

Terrestrial stromatolites present opportunities for chiral analysis because of the preservation of organic material and associated mineral phases (136–139). However, detection of similar signatures in extraterrestrial samples is more challenging because of limited preservation and alteration in harsh environments. The Martian meteorite ALH84001, for example, has been studied for potential fossil-like features and organic compounds such as polycyclic aromatic hydrocarbons, though interpretations remain contested (140, 141).

Traditional microscopy and spectroscopic techniques may be insufficient to confirm biogenetic origin in these contexts. VCD offers a complementary method by enabling the detection of molecular chirality associated with bacterial residues or biominerals, even when morphological evidence is ambiguous. This approach may be especially useful for analyzing samples either returned to Earth or examined in situ on planetary surfaces.

To date, most chirality studies have relied on meteorites that have impacted Earth, where terrestrial contamination is difficult to rule out. In situ chirality measurements would help overcome this limitation. QCL-based VCD systems are particularly well-suited for space missions because of their small size, low power requirements, and rapid data acquisition, enabling chirality analysis in environments such as the lunar surface, asteroids, or Martian regolith that were previously inaccessible to conventional instrumentation.

7. THE FUTURE OF QUANTUM CASCADE LASER–BASED VIBRATIONAL CIRCULAR DICHROISM

The future of QCL-VCD microscopy systems is promising, driven by advances in metamaterials and computational methods that will allow for more robust VCD applications in the near future. A fully integrated, laboratory-grade benchtop QCL-VCD microscopy system is on the horizon; it will allow researchers to explore the untapped potential of chiroptical microscopy across various fields, in a very similar manner to FT-IR microscopy more than 40 years ago. This section discusses recent advances in optical metamaterials and machine learning, as well as their potential integration into future QCL-VCD applications.

7.1. Quantum Cascade Laser Advances and Schemes

The development and commercialization of QCLs have transformed mid-IR spectroscopy, offering compact, high-power, and tunable light sources well-suited for VCD. As their performance and availability continue to improve, QCLs will present new opportunities to overcome the long-standing limitations of traditional VCD instrumentation, particularly in terms of spectral reach, signal strength, and system integration.

Commercialization of QCLs has significantly broadened their applicability in VCD, driven by both wider spectral coverage and increased output power. Modern commercial QCLs now range from 3 to 20 μm, enabling access to molecular vibrational bands in the 3 μm ($\sim$3,300 cm^{-1}) region—such as O–H and N–H stretches—and rotational molecular bands in the far-IR region that were previously inaccessible with conventional mid-IR sources (51, 142). This extension allows VCD investigations of functional groups and biological molecules with richer spectral detail. Furthermore, commercially available QCLs offer high CW and pulsed powers, ranging from tens of milliwatts to several watts, as a result of improved semiconductor design, packaging, and

thermal handling (143). Higher power directly improves SNR, enables longer path lengths, and extends sensitivity in highly absorbing or dilute samples—ideal for biological and trace analyte VCD applications.

Additionally, recent technological advancements have expanded the utility of QCLs beyond single-wavelength operation. In particular, QCL frequency combs enable the simultaneous emission of multiple evenly spaced wavelengths, opening the door to interferometric approaches within QCL-VCD instrumentation. These comb sources can be integrated into FT-VCD systems, analogous to their use in dual-comb spectroscopy, where two combs with slightly offset repetition rates generate a time-domain interferogram without moving parts (144). This approach offers the potential for significantly faster acquisition, improved SNR, and enhanced spectral resolution, positioning dual-comb QCLs as a powerful tool for next-generation VCD.

Recent advances have enabled the integration of QCLs onto silicon photonic platforms, offering a promising route toward chip-scale systems. Such miniaturization drastically reduces the system's footprint and power consumption, making QCL-VCD viable for lab-on-a-chip technologies in energy- or space-constrained environments such as portable diagnostics or space missions. Moreover, compatibility with CMOS fabrication processes—well-established in the semiconductor industry—opens the door to mass production of QCLs, which would significantly reduce cost and enhance accessibility for broader adoption of QCL-based VCD instrumentation.

Combined, these advances position modern QCLs as robust, tunable, and powerful mid-IR sources. As devices tailored for spectroscopy, they lower the barrier to VCD implementation in academic, industrial, and field environments, making high-performance QCL-VCD both technically reliable and commercially accessible for a wide range of analytical applications. Together, these technological developments, including broader spectral coverage, higher power output, frequency comb operation, and chip-scale integration, establish QCLs as versatile and scalable light sources for next-generation VCD. Their compatibility with mass-manufacturing platforms and suitability for compact, high-performance spectroscopic systems pave the way for widespread adoption of QCL-based VCD in both research and commercial settings.

7.2. Machine Learning

Machine learning has rapidly become a powerful adjunct to both imaging and spectroscopy, offering new ways to enhance spatial resolution and automate spectral interpretation in VCD. In imaging, deep learning–based superresolution methods now routinely outperform bicubic interpolation: Networks trained on large data sets or even on single low-resolution images subdivided into patches can reconstruct subcellular detail with micrometer-scale precision (145–147). Preliminary research in VCD has applied neural nets to near-IR spectra for baseline correction and enantiomeric discrimination, demonstrating that machine learning can extract subtle chiral features from noisy data (148, 149). Together, these advances suggest that the integration of machine learning–driven denoising, superresolution, and spectral unmixing into QCL-VCD imaging workflows could substantially boost both sensitivity and spatial fidelity.

8. CONCLUSION

In this review article, we have provided a comprehensive instrumentation overview of the field of QCL-VCD spectroscopy and microscopy. While current research and instrumentation configurations have produced usable, high-definition, high-SNR spectra, significant research must still be performed before we have a full understanding of the QCL-VCD system. Further analysis of what assumptions can or cannot be carried over from the FT-VCD predecessor must be done.

Exposure times must be reduced and a more robust chemical data set must be made before QCL-VCD systems can be used as ubiquitously as FT-IR systems. But with the evolving landscape of QCL architectures and output characteristics, advances in signal-processing methodologies, and novel optical materials, it does not seem unreasonable to imagine an integrated QCL-VCD system coming to fruition in the near future.

SUMMARY POINTS

1. Quantum-cascade lasers (QCLs) provide high-power, tunable mid-IR illumination that dramatically improves signal-to-noise ratios in vibrational circular dichroism (VCD) spectroscopy.
2. Integration of QCL sources into VCD imaging platforms is nontrivial. Their high power and beam characteristics require polarization-modulation elements, particularly photoelastic modulators (PEMs), to be reengineered for modulation depth as well as synchronization in order to maintain baseline stability and artifact suppression.
3. Raster-scanned QCL-VCD imaging achieves micrometer-scale spatial resolution, enabling label-free mapping of chiral structures in biological tissues, pharmaceuticals, and materials.
4. Integration of rapid wavelength switching and advanced data-processing pipelines permits near-real-time acquisition of VCD images with both high spectral fidelity and spatial clarity.

FUTURE ISSUES

1. The development of compact, turnkey QCL-VCD spectrometers and microscopes suitable for point-of-care or field deployment in clinical and environmental settings is a key future direction.
2. Machine learning algorithms will be implemented to deconvolute overlapping chiral signatures and automate quantitative analysis in complex biological samples.
3. Nonlinear chiroptical extensions, such as second-harmonic-generation VCD, will be explored to access complementary contrast mechanisms and enable deeper tissue penetration.
4. Calibration protocols and reference materials will be standardized to ensure reproducibility and comparability of QCL-VCD imaging results across laboratories.

DISCLOSURE STATEMENT

The authors are not aware of any affiliations, memberships, funding, or financial holdings that might be perceived as affecting the objectivity of this review.

ACKNOWLEDGMENTS

We gratefully acknowledge the National Science Foundation (Partnership for Innovation Program via grant 2414684) and the National Aeronautics and Space Administration (PICASSO

program via grant 23-PICASSO23-0026). V.A.N. appreciates the support provided by a Clare Booth Luce Fellowship. The authors thank Roya Akrami for contributions to figure development as well as Prof. Prasad Polavarapu and Dr. Rina Dukor for useful discussions.

LITERATURE CITED

1. Keiderling TA. 1996. Vibrational circular dichroism: applications to conformational analysis of biomolecules. In *Circular Dichroism and the Conformational Analysis of Biomolecules*, ed. GD Fasman. Springer
2. Moffitt W. 1956. The optical rotatory dispersion of simple polypeptides. II. *PNAS* 42(10):736–46
3. Hunt HD, Simpson WT. 1953. Spectra of simple amides in the vacuum ultraviolet. *J. Am. Chem. Soc.* 75(18):4540–43
4. Yang JT, Doty P. 1957. The optical rotatory dispersion of polypeptides and proteins in relation to configuration. *J. Am. Chem. Soc.* 79(4):761–75
5. Greenfield NJ, Fasman GD. 1969. Computed circular dichroism spectra for the evaluation of protein conformation. *Biochemistry* 8(10):4108–16
6. Stephens PJ, Lowe MA. 1985. Vibrational circular dichroism. *Annu. Rev. Phys. Chem.* 36:213–41
7. Hsu EC, Holzwarth G. 1973. Vibrational circular dichroism observed in crystalline α-$NiSO_4 \cdot 6H_2O$ and α-$ZnSeO_4 \cdot 6H_2O$ between 1900 and 5000 cm^{-1} . *J. Chem. Phys.* 59(9):4678–85
8. Kemp JC. 1969. Piezo-optical birefringence modulators: new use for a long-known effect. *J. Opt. Soc. Am.* 59(8):950–54
9. Cheng JC, Nafie LA, Stephens PJ. 1975. Polarization scrambling using a photoelastic modulator: application to circular dichroism measurement. *J. Opt. Soc. Am.* 65(9):1031–35
10. Keiderling TA, Lakhani A. 2018. Mini review: instrumentation for vibrational circular dichroism spectroscopy, still a role for dispersive instruments. *Chirality* 30(3):238–53
11. Keiderling TA. 2018. Instrumentation for vibrational circular dichroism spectroscopy: method comparison and newer developments. *Molecules* 23(9):2404
12. Nafie LA, Diem M, Vidrine DW. 1979. Fourier transform infrared vibrational circular dichroism. *J. Am. Chem. Soc.* 101(2):496–98
13. Nafie LA, Diem M. 1979. Theory of high frequency differential interferometry: application to the measurement of infrared circular and linear dichroism via Fourier transform spectroscopy. *Appl. Spectrosc.* 33(2):130–35
14. Polavarapu PL, Chen GC, Weibel S. 1994. Development, justification, and applications of a mid-infrared polarization-division interferometer. *Appl. Spectrosc.* 48(10):1224–35
15. Polavarapu PL, Deng Z, Chen GC. 1995. Polarization-division interferometry: time-resolved infrared vibrational dichroism spectroscopy. *Appl. Spectrosc.* 49(2):229–36
16. Arrunategui Norvick V, Le M, Modesitt E, Myers O, Akrami R, Phal Y. 2025. Rapid vibrational circular dichroism spectroscopy via synchronized photoelastic modulator–quantum cascade laser integration. *ACS Meas. Sci. Au* 5(5):729–39
17. Griffiths PR. 1983. Fourier transform infrared spectrometry. *Science* 222(4621):297–302
18. Nafie LA. 2000. Dual polarization modulation: a real-time, spectral-multiplex separation of circular dichroism from linear birefringence spectral intensities. *Appl. Spectrosc.* 54(11):1634–45
19. Keiderling TA. 1981. Vibrational circular dichroism. *Appl. Spectrosc. Rev.* 17(2):189–226
20. Nafie LA. 2012. Infrared vibrational optical activity: measurement and instrumentation. *Compr. Chiropt. Spectrosc.* 1:115–46
21. Lu X, Li H, Nafie JW, Pazderka T, Pazderková M, et al. 2017. A vibrational circular dichroism microsampling accessory: mapping enhanced vibrational circular dichroism in amyloid fibril films. *Appl. Spectrosc.* 71(6):1117–26
22. Su CN, Heintz VJ, Keiderling TA. 1980. Vibrational circular dichroism in the mid-infrared. *Chem. Phys. Lett.* 73(1):157–59
23. Lipp ED, Zimba CG, Nafie LA. 1982. Vibrational circular dichroism in the mid-infrared using Fourier transform spectroscopy. *Chem. Phys. Lett.* 90(1):1–5

24. Brandstetter M, Koch C, Genner A, Lendl B. 2014. Measures for optimizing pulsed EC-QC laser spectroscopy of liquids and application to multi-analyte blood analysis. *Proc. SPIE* 8993:283–93
25. Alcaráz MR, Schwaighofer A, Goicoechea H, Lendl B. 2016. EC-QCL mid-IR transmission spectroscopy for monitoring dynamic changes of protein secondary structure in aqueous solution on the example of β-aggregation in alcohol-denaturated α-chymotrypsin. *Anal. Bioanal. Chem.* 408:3933–41
26. Kuligowski J, Schwaighofer A, Alcaráz MR, Quintás G, Mayer H, et al. 2017. External cavity–quantum cascade laser (EC-QCL) spectroscopy for protein analysis in bovine milk. *Anal. Chim. Acta* 963:99–105
27. Akhgar CK, Ramer G, Żbik M, Trajnerowicz A, Pawluczyk J, et al. 2020. The next generation of IR spectroscopy: EC-QCL-based mid-IR transmission spectroscopy of proteins with balanced detection. *Anal. Chem.* 92(14):9901–7
28. Brandstetter M, Lendl B. 2012. Tunable mid-infrared lasers in physical chemosensors: towards the detection of physiologically relevant parameters in biofluids. *Sens. Actuators B* 170:189–95
29. Rüther A, Pfeifer M, Lórenz-Fonfría VA, Lüdeke S. 2014. Reaction monitoring using mid-infrared laser-based vibrational circular dichroism. *Chirality* 26(9):490–96
30. Kübel JM, Botha C, Bucka A, Höpfner J, Zimmermann H, et al. 2019. A new quantum cascade IR-laser online detector: chemical-sensitive size-exclusion chromatography measurement at unprecedented low levels. *Macromol. Rapid Commun.* 40(18):1900228
31. Waclawek JP, Kristament C, Moser H, Lendl B. 2019. Balanced-detection interferometric cavity-assisted photothermal spectroscopy. *Opt. Express* 27(9):12183–95
32. Hermann DR, Ramer G, Kitzler-Zeiler M, Lendl B. 2022. Quantum cascade laser–based vibrational circular dichroism augmented by a balanced detection scheme. *Anal. Chem.* 94(29):10384–90
33. Celebrano M, Kukura P, Renn A, Sandoghdar V. 2011. Single-molecule imaging by optical absorption. *Nat. Photonics* 5(2):95–98
34. Tittel F, Lewicki R. 2013. Tunable mid-infrared laser absorption spectroscopy. In *Semiconductor Lasers: Fundamentals and Applications*, ed. A Baranov, E Tournié. Elsevier
35. Durry G, Pouchet I, Amarouche N, Danguy T, Megie G. 2000. Shot-noise-limited dual-beam detector for atmospheric trace-gas monitoring with near-infrared diode lasers. *Appl. Opt.* 39(30):5609–19
36. Hobbs PC. 1991. Shot noise limited optical measurements at baseband with noisy lasers. *Proc. SPIE* 1376:216–21
37. Hobbs PC. 1997. Ultrasensitive laser measurements without tears. *Appl. Opt.* 36(4):903–20
38. Masciotti JM, Lasker JM, Hielscher AH. 2008. Digital lock-in detection for discriminating multiple modulation frequencies with high accuracy and computational efficiency. *IEEE Trans. Instrum. Meas.* 57(1):182–89
39. Qin J, Huang Z, Ge Y, Hou Y, Chu J. 2009. Tandem demodulation lock-in amplifier based on digital signal processor for dual-modulated spectroscopy. *Rev. Sci. Instrum.* 80:033112
40. de Graaf G, Wolffenbuttel R. 2012. Lock-in amplifier techniques for low-frequency modulated sensor applications. In *2012 IEEE International Instrumentation and Measurement Technology Conference Proceedings*. IEEE
41. Fu S, Sakurai A, Liu L, Edman F, Pullerits T, et al. 2013. Generalized lock-in amplifier for precision measurement of high frequency signals. *Rev. Sci. Instrum.* 84:115101
42. Nafie LA. 2011. Instrumentation for vibrational circular dichroism. In *Vibrational Optical Activity: Principles and Applications*, ed. LA Nafie. John Wiley & Sons, Inc.
43. Hermann DR, Ramer G, Riedlsperger L, Lendl B. 2023. Chiral monitoring across both enantiomeric excess and concentration space: leveraging quantum cascade lasers for sensitive vibrational circular dichroism spectroscopy. *Appl. Spectrosc.* 77(12):1362–70
44. Phal Y, Yeh K, Bhargava R. 2020. Concurrent vibrational circular dichroism measurements with infrared spectroscopic imaging. *Anal. Chem.* 93(3):1294–303
45. Phal Y, Yeh K, Bhargava R. 2021. Chirality mapping in microscopy format. *Opt. Photonics News* 32(12):30–31
46. Nafie LA, Buijs H, Rilling A, Cao X, Dukor RK. 2004. Dual source Fourier transform polarization modulation spectroscopy: an improved method for the measurement of circular and linear dichroism. *Appl. Spectrosc.* 58(6):647–54

47. Freedman TB, Cao X, Dukor RK, Nafie LA. 2003. Absolute configuration determination of chiral molecules in the solution state using vibrational circular dichroism. *Chirality* 15(9):743–58
48. Wang B, Leadbetter A, Rockwell RR. 2005. Evaluation of a dual PEM Stokes polarimeter using different signal processing methods. *Proc. SPIE* 5888:251–58
49. Sato H, Shimizu M, Watanabe K, Yoshida J, Kawamura I, Koshoubu J. 2021. Multidimensional vibrational circular dichroism apparatus equipped with quantum cascade laser and its use for investigating some peptide systems containing D-amino acids. *Anal. Chem.* 93(5):2742–48
50. Schwaighofer A, Brandstetter M, Lendl B. 2017. Quantum cascade lasers (QCLs) in biomedical spectroscopy. *Chem. Soc. Rev.* 46(19):5903–24
51. Faist J. 2013. *Quantum Cascade Lasers*. Oxford University Press. 1st ed.
52. Kazarinov R, Suris R. 1971. Possible amplification of electromagnetic waves in a semiconductor with a superlattice. *Fiz. Tekh. Poluprovodn.* 5:797–800
53. Faist J, Capasso F, Sivco DL, Sirtori C, Hutchinson AL, Cho AY. 1994. Quantum cascade laser. *Science* 264(5158):553–56
54. Gmachl C, Capasso F, Sivco DL, Cho AY. 2001. Recent progress in quantum cascade lasers and applications. *Rep. Prog. Phys.* 64(11):1533–601
55. Vurgaftman I. 2020. Superlattice and quantum-well band structure. In *Bands and Photons in III–V Semiconductor Quantum Structures*, ed. I Vurgaftman, MP Lumb, JR Meyer. Oxford University Press
56. Fox M, Ispasoiu R. 2017. Quantum wells, superlattices, and band-gap engineering. In *Springer Handbook of Electronic and Photonic Materials*, ed. P Capper, S Kasap. Springer
57. Hugi A, Maulini R, Faist J. 2010. External cavity quantum cascade laser. *Semicond. Sci. Technol.* 25:083001
58. Faist J, Capasso F, Sirtori C, Sivco DL, Baillargeon JN, et al. 1996. High power mid-infrared ($\lambda \sim 5$ μm) quantum cascade lasers operating above room temperature. *Appl. Phys. Lett.* 68(26):3680–82
59. Diehl L, Pflügl C, Witinski M, Wang P, Tague T, Capasso F. 2010. Fourier transform spectrometers utilizing mid-infrared quantum cascade lasers. In *CLEO/QELS: 2010 Laser Science to Photonic Applications*. IEEE
60. Faist J, Gmachl C, Capasso F, Sirtori C, Sivco DL, et al. 1997. Distributed feedback quantum cascade lasers. *Appl. Phys. Lett.* 70(20):2670–72
61. Gmachl C, Faist J, Bailargeon J, Capasso F, Sirtori C, et al. 1997. Complex-coupled quantum cascade distributed-feedback laser. *IEEE Photonics Technol. Lett.* 9(8):1090–92
62. Namjou K, Cai S, Whittaker EA, Faist J, Gmachl C, et al. 1998. Sensitive absorption spectroscopy with a room-temperature distributed-feedback quantum-cascade laser. *Opt. Lett.* 23(3):219–21
63. Wittmann A, Bonetti Y, Fischer M, Faist J, Blaser S, Gini E. 2009. Distributed-feedback quantum-cascade lasers at 9 μm operating in continuous wave up to 423 K. *IEEE Photonics Technol. Lett.* 21(12):814–16
64. Lee BG, Belkin MA, Pflügl C, Diehl L, Zhang HA, et al. 2009. DFB quantum cascade laser arrays. *IEEE J. Quantum Electron.* 45(5):554–65
65. Lee BG, Zhang HA, Pflügl C, Diehl L, Belkin MA, et al. 2009. Broadband distributed-feedback quantum cascade laser array operating from 8.0 to 9.8 μm. *IEEE Photonics Technol. Lett.* 21(13):914–16
66. Ma Y, Ding K, Wei L, Li X, Shi J, et al. 2022. Research on mid-infrared external cavity quantum cascade lasers and applications. *Crystals* 12(11):1564
67. Luo G, Peng C, Le H, Pei S, Hwang WY, et al. 2001. Grating-tuned external-cavity quantum-cascade semiconductor lasers. *Appl. Phys. Lett.* 78(19):2834–36
68. Wittmann A, Gresch T, Gini E, Hvozdara L, Hoyler N, et al. 2007. High-performance bound-to-continuum quantum-cascade lasers for broad-gain applications. *IEEE J. Quantum Electron.* 44(1):36–40
69. Wysocki G, Curl RF, Tittel FK, Maulini R, Bulliard JM, Faist J. 2005. Widely tunable mode-hop free external cavity quantum cascade laser for high resolution spectroscopic applications. *Appl. Phys. B* 81:769–77
70. Bayrakli I. 2022. Double-mode external cavity quantum cascade lasers. *Opt. Quantum Electron.* 54(7):425
71. Mohan A, Wittmann A, Hugi A, Blaser S, Giovannini M, Faist J. 2007. Room-temperature continuous-wave operation of an external-cavity quantum cascade laser. *Opt. Lett.* 32(19):2792–94
72. Wittmann A, Hugi A, Gini E, Hoyler N, Faist J. 2008. Heterogeneous high-performance quantum-cascade laser sources for broad-band tuning. *IEEE J. Quantum Electron.* 44(11):1083–88

73. Maulini R, Beck M, Faist J, Gini E. 2004. Broadband tuning of external cavity bound-to-continuum quantum-cascade lasers. *Appl. Phys. Lett.* 84(10):1659–61
74. Maulini R, Mohan A, Giovannini M, Faist J, Gini E. 2006. External cavity quantum-cascade laser tunable from 8.2 to 10.4 μm using an inhomogenously broadened gain element. In *2006 Conference on Lasers and Electro-Optics and 2006 Quantum Electronics and Laser Science Conference*. IEEE
75. Hugi A, Terazzi R, Bonetti Y, Wittmann A, Fischer M, et al. 2009. External cavity quantum cascade laser tunable from 7.6 to 11.4 μm. *Appl. Phys. Lett.* 95:061103
76. Lüdeke S, Pfeifer M, Fischer P. 2011. Quantum-cascade laser–based vibrational circular dichroism. *J. Am. Chem. Soc.* 133(15):5704–7
77. Sato H, Shimizu M, Watanabe K, Yoshida J, Kawamura I, Koshoubu J. 2021. Vibrational circular dichroism system equipped with quantum cascade laser for microscopic scanning. *Chem. Lett.* 50(8):1543–45
78. Phal Y, Yeh K, Bhargava R. 2021. Discrete frequency infrared vibrational circular dichroism spectroscopy & imaging. In *Proceedings of Novel Techniques in Microscopy*. Optica Publishing Group
79. Lakhani A, Malon P, Keiderling TA. 2009. Comparison of vibrational circular dichroism instruments: development of a new dispersive VCD. *Appl. Spectrosc.* 63(7):775–85
80. Coldren L. 2012. *Diode Lasers and Photonic Integrated Circuits*. John Wiley & Sons, Inc. 1st ed.
81. Phal Y, Yeh K, Bhargava R. 2020. Polarimetric infrared spectroscopic imaging using quantum cascade lasers. *Proc. SPIE* 11252:36–45
82. Phal Y, Yeh K, Bhargava R. 2021. Design considerations for discrete frequency infrared microscopy systems. *Appl. Spectrosc.* 75(9):1067–92
83. Colombelli R, Capasso F, Gmachl C, Hutchinson AL, Sivco DL, et al. 2001. Far-infrared surface-plasmon quantum-cascade lasers at 21.5 μm and 24 μm wavelengths. *Appl. Phys. Lett.* 78(18):2620–22
84. Dhillon S, Alton J, Barbieri S, Sirtori C, De Rossi A, et al. 2005. Ultralow threshold current terahertz quantum cascade lasers based on double-metal buried strip waveguides. *Appl. Phys. Lett.* 87:071107
85. Wang B, List J. 2005. Basic optical properties of the photoelastic modulator. Part I. Useful aperture and acceptance angle. *Proc. SPIE* 5888:58881I
86. Cheng J, Nafie L, Allen SD, Braunstein A. 1976. Photoelastic modulator for the 0.55–13-μm range. *Appl. Opt.* 15(8):1960–65
87. Hipps KW, Crosby GA. 1979. Applications of the photoelastic modulator to polarization spectroscopy. *J. Phys. Chem.* 83(5):555–62
88. Canit JC, Badoz J. 1983. New design for a photoelastic modulator. *Appl. Opt.* 22(4):592–94
89. Badoz J, Billardon M, Boccara A, Briat B. 1969. Measurement and interpretation of magnetic circular dichroism and magnetic linear dichroism spectra. *Symp. Faraday Soc.* 3:27–39
90. Mollenauer LF, Downie D, Engstrom H, Grant WB. 1969. Stress plate optical modulator for circular dichroism measurements. *Appl. Opt.* 8(3):661–65
91. Bai Y, Slivken S, Darvish SR, Razeghi M. 2008. Room temperature continuous wave operation of quantum cascade lasers with 12.5% wall plug efficiency. *Appl. Phys. Lett.* 93:021103
92. Bai Y, Bandyopadhyay N, Tsao S, Slivken S, Razeghi M. 2011. Room temperature quantum cascade lasers with 27% wall plug efficiency. *Appl. Phys. Lett.* 98:181102
93. Finkman E, Nemirovsky Y. 1979. Infrared optical absorption of $Hg_{1-x}Cd_xTe$. *J. Appl. Phys.* 50(6):4356–61
94. Shen SC. 1994. Comparison and competition between MCT and QW structure material for use in IR detectors. *Microelectron. J.* 25(8):713–39
95. Reine MB. 2001. Photovoltaic detectors in MCT. In *Infrared Detectors and Emitters: Materials and Devices*, ed. P Capper, CT Elliott. Springer
96. Hansen GL, Schmit JL. 1983. Calculation of intrinsic carrier concentration in $Hg_{1-x}Cd_xTe$. *J. Appl. Phys.* 54(3):1639–40
97. Gawron W, Kebłowski A, Kopytko M, Madejczyk P, Martyniuk P, et al. 2016. Recent progress in LWIR HOT photoconductors based on MOCVD grown (100) HgCdTe. *J. Phys. D* 31:105004
98. Sze SM, Ng KK. 2002. HgCdTe infrared detectors: growth, fabrication, and applications. *J. Vacuum Sci. Technol. B* 20(4):1234–42

99. Gawron W, Sobieski J, Manyk T, Kopytko M, Madejczyk P, Rutkowski J. 2021. MOCVD grown HgCdTe heterostructures for medium wave infrared detectors. *Coatings* 11(5):611
100. Eich D, Schirmacher W, Hanna S, Mahlein KM, Fries P, Figgemeier H. 2017. Progress of MCT detector technology at AIM towards smaller pitch and lower dark current. *J. Electron. Mater.* 46(9):5448–57
101. McMaster WH. 1961. Matrix representation of polarization. *Rev. Mod. Phys.* 33(1):8–28
102. Stephens PJ. 1985. Theory of vibrational circular dichroism. *J. Phys. Chem.* 89(5):748–52
103. Nafie LA. 2020. Vibrational optical activity: from discovery and development to future challenges. *Chirality* 32(5):667–92
104. Vap JC, Nauyoks SE, Benson MR, Marciniak MA. 2017. Use of a novel infrared wavelength-tunable laser Mueller-matrix polarimetric scatterometer to measure nanostructured optical materials. *Rev. Sci. Instrum.* 88:103104
105. Janassek P, Hartmann S, Molitor A, Michel F, Elsäßer W. 2016. Investigations of the polarization behavior of quantum cascade lasers by Stokes parameters. *Opt. Lett.* 41(2):305–8
106. Goldstein DH. 2003. The Mueller matrices for polarizing components. In *Polarized Light, Revised and Expanded*. CRC Press. 2nd ed.
107. Keiderling TA. 2020. Structure of condensed phase peptides: insights from vibrational circular dichroism and Raman optical activity techniques. *Chem. Rev.* 120(7):3381–419
108. Pancoska P, Bitto E, Janota V, Keiderling TA. 1994. Quantitative analysis of vibrational circular dichroism spectra of proteins: problems and perspectives. *Faraday Discuss.* 99:287–310
109. Pancoska P, Bitto E, Janota V, Urbanova M, Gupta VP, Keiderling TA. 1995. Comparison of and limits of accuracy for statistical analyses of vibrational and electronic circular dichroism spectra in terms of correlations to and predictions of protein secondary structure. *Protein Sci.* 4(7):1384–401
110. Pancoska P, Keiderling TA. 1991. Systematic comparison of statistical analyses of electronic and vibrational circular dichroism for secondary structure prediction of selected proteins. *Biochemistry* 30(28):6885–95
111. Baumruk V, Keiderling TA. 1993. Vibrational circular dichroism of proteins in water solution. *J. Am. Chem. Soc.* 115(15):6939–42
112. Baumruk V, Pancoska P, Keiderling TA. 1996. Predictions of secondary structure using statistical analyses of electronic and vibrational circular dichroism and Fourier transform infrared spectra of proteins in H_2O. *J. Mol. Biol.* 259(4):774–91
113. Ma S, Freedman TB, Dukor RK, Nafie LA. 2010. Near-infrared and mid-infrared Fourier transform vibrational circular dichroism of proteins in aqueous solution. *Appl. Spectrosc.* 64(6):615–26
114. Jeong Y, Hsieh PH, Phal Y, Bhargava R, Irudayaraj J. 2024. Label-free monitoring of coculture system dynamics: probing probiotic and cancer cell interactions via infrared spectroscopic imaging. *Anal. Chem.* 96(28):11247–54
115. Hsieh PH, Phal Y, Bhargava R. 2022. Cell phase identification in a three-dimensional engineered tumor model by infrared spectroscopic imaging. *Anal. Chem.* 94(56):2349–57
116. Dukor RK, Pancoska P, Keiderling TA, Prestrelski SJ, Arakawa T. 1992. Vibrational circular dichroism studies of epidermal growth factor and basic fibroblast growth factor. *Arch. Biochem. Biophys.* 298(2):678–81
117. Singh RS, Palmer JC, Pudney PDA, Paul PKC, Johannessen C, et al. 2017. Molecular modeling and structural characterization of a high glycine–tyrosine hair keratin associated protein. *Phys. Chem. Chem. Phys.* 19(12):8575–83
118. Shanmugam G, Polavarapu PL. 2006. Structures of intact glycoproteins from vibrational circular dichroism. *Proteins Struct. Funct. Bioinform.* 63(4):768–76
119. Yasui SC, Pancoska P, Dukor RK, Keiderling TA, Renugopalakrishnan V, et al. 1990. Conformational transitions in phosvitin with pH variation: vibrational circular dichroism study. *J. Biol. Chem.* 265(7):3780–88
120. Keiderling TA, Wang B, Urbanova M, Pancoska P, Dukor RK. 1994. Empirical studies of protein secondary structure by vibrational circular dichroism and related techniques: α-lactalbumin and lysozyme as examples. *Faraday Discuss.* 99:263–85
121. Xu Q, Keiderling TA. 2004. Optical spectroscopic differentiation of various equilibrium denatured states of horse cytochrome *c*. *Biopolymers* 73(6):716–26

122. Kurouski D. 2017. Advances of vibrational circular dichroism (VCD) in bioanalytical chemistry: a review. *Anal. Chim. Acta* (990):54–66
123. Wang L, Keiderling TA. 1993. Helical nature of poly(dl-dC).poly(dl-dC): vibrational circular dichroism results. *Nucleic Acids Res.* 21(17):4127–32
124. Andrushchenko V, Van De Sande JH, Wieser H. 2003. Vibrational circular dichroism and IR absorption of DNA complexes with Cu^{2+} ions. *Biopolymers* 72(5):374–90
125. Lin GQ, Zhang JG, Cheng JF. 2011. Overview of chirality and chiral drugs. In *Chiral Drugs: Chemistry and Biological Action*, ed. GQ Lin, QD You, JF Cheng. John Wiley & Sons, Inc.
126. Wesolowski SS, Pivonka DE. 2013. A rapid alternative to X-ray crystallography for chiral determination: case studies of vibrational circular dichroism (VCD) to advance drug discovery projects. *Bioorg. Med. Chem. Lett.* 23(14):4019–25
127. Elmore CS, Dorff PN, Powell ME, Hall JE, Simpson TR. 2011. Synthesis of the NK3 receptor antagonist AZD2624 in C-14-, H-3- and C-13-labeled forms. *J. Label. Compd. Radiopharm.* 54(5):239–46
128. Sklenář A, Růžičková L, Schrenková V, Bednárová L, Pazderková M, et al. 2024. Solid-state vibrational circular dichroism for pharmaceutical applications: polymorphs and cocrystal of sofosbuvir. *Spectrochim. Acta A* 318:124478
129. Bonner WA. 2000. Parity violation and the evolution of biomolecular homochirality. *Chirality* 12(3):114–26
130. Bonner WA. 1988. Origins of chiral homogeneity in nature. In *Topics in Stereochemistry*, Vol. 18, ed. EL Eliel, SH Wilen. John Wiley & Sons, Inc.
131. Glavin DP, Burton AS, Elsila JE, Aponte JC, Dworkin JP. 2020. The search for chiral asymmetry as a potential biosignature in our solar system. *Chem. Rev.* 120(11):4660–89
132. Bocková J, Jones NC, Meierhenrich UJ, Hoffmann SV, Meinert C. 2021. Chiroptical activity of hydroxycarboxylic acids with implications for the origin of biological homochirality. *Commun. Chem.* 4(1):86
133. Shoji M, Kitazawa Y, Sato A, Watanabe N, Boero M, et al. 2023. Enantiomeric excesses of aminonitrile precursors determine the homochirality of amino acids. *J. Phys. Chem. Lett.* 14(13):3243–48
134. Albano G, Pescitelli G, Di Bari L. 2020. Chiroptical properties in thin films of π-conjugated systems. *Chem. Rev.* 120(18):10145–43
135. Barghoorn ES, Schopf JW. 1966. Microorganisms three billion years old from the Precambrian of South Africa. *Science* 152(3723):758–63
136. Kühl M, Behrendt L, Trampe ECL, Qvortrup K, Schreiber U, et al. 2012. Microenvironmental ecology of the chlorophyll *b*–containing symbiotic cyanobacterium *Prochloron* in the didemnid ascidian *Lissoclinum patella*. *Front. Microbiol.* 3:1–18
137. Zhang XG, Pratt BR. 2014. Possible algal origin and life cycle of Ediacaran Doushantuo microfossils with dextral spiral structure. *J. Paleontol.* 88(1):92–98
138. Sato H, Yoshida J, Yamagishi A. 2024. VCD of inorganic supramolecular chirality. In *Multi-Dimensional Vibrational Circular Dichroism*. Springer
139. McGeoch JEM, Frommelt AJ, Owen RL, Cinque G, McClelland A, et al. 2024. Fossil and present-day stromatolite ooids contain a meteoritic polymer of glycine and iron. *Int. J. Astrobiol.* 23:e20
140. Jiang W, Yi X, McKee MD. 2019. Chiral biomineralized structures and their biomimetic synthesis. *Mater. Horiz.* 6(10):1974–90
141. Jiang W, Pacella MS, Vali H, Gray JJ, McKee MD. 2018. Chiral switching in biomineral suprastructures induced by homochiral L-amino acid. *Sci. Adv.* 4(8):eaas9819
142. Vitiello MS, Scalari G, Williams B, De Natale P. 2015. Quantum cascade lasers: 20 years of challenges. *Opt. Express* 23(4):5167–82
143. Rogalski A. 2019. Infrared and terahertz detectors: advances, challenges, and applications. *Opto-Electron. Rev.* 27(2):127–49
144. Villares G, Hugi A, Blaser S, Faist J. 2014. Dual-comb spectroscopy based on quantum-cascade–laser frequency combs. *Nat. Commun.* 5:5192
145. Wang Z, Chen J, Hoi SCH. 2021. Deep learning for image super-resolution: a survey. *IEEE Trans. Pattern Anal. Mach. Intell.* 43(10):3365–87

146. Ledig C, Theis L, Huszar F, Caballero J, Cunningham A, et al. 2017. Photo-realistic single image super-resolution using a generative adversarial network. In *2017 IEEE Conference on Computer Vision and Pattern Recognition* (*CVPR*). IEEE
147. Lim B, Son S, Kim H, Nah S, Lee KM. 2017. Enhanced deep residual networks for single image super-resolution. In *2017 IEEE Conference on Computer Vision and Pattern Recognition* (*CVPR*). IEEE
148. Acquarelli J, van Laarhoven T, Gerretzen J, Tran TN, Buydens LMC, Marchiori E. 2017. Convolutional neural networks for vibrational spectroscopic data analysis. *Anal. Chim. Acta* 954:22–31
149. Yang J, Xu J, Zhang X, Wu C, Lin T, Ying Y. 2019. Deep learning for vibrational spectral analysis: recent progress and a practical guide. *Anal. Chim. Acta* 1081:6–17
150. Utyushev A, Rasskazov I, Phal Y. 2026. Transfer-matrix framework for modeling mid-infrared vibrational circular dichroism spectra. *Anal. Chem*. **https://doi.org/10.1021/acs.analchem.5c07726**